

# Adaptive diffusion constrained total variation scheme with application to ‘cartoon + texture + edge’ image decomposition\*

Juan C. Moreno<sup>†</sup>   V. B. Surya Prasath<sup>‡</sup>   D. Vorotnikov<sup>§</sup>   Hugo Proença<sup>¶</sup>  
K. Palaniappan<sup>||</sup>

## Abstract

We consider an image decomposition model involving a variational (minimization) problem and an evolutionary partial differential equation (PDE). We utilize a linear inhomogeneous diffusion constrained and weighted total variation (TV) scheme for image adaptive decomposition. An adaptive weight along with TV regularization splits a given image into three components representing the geometrical (cartoon), textural (small scale - microtextures), and edges (big scale - macrotextures). We study the wellposedness of the coupled variational-PDE scheme along with an efficient numerical scheme based on Chambolle’s dual minimization [14]. We provide extensive experimental results in cartoon-texture-edges decomposition, and denoising as well compare with other related variational, coupled anisotropic diffusion PDE based methods.

**Keywords:** Image decomposition, total variation, linear diffusion, adaptive weights, multi-scale, denoising.

## 1 Introduction

Decomposing an image into meaningful components is an important and challenging inverse problem in image processing. Image denoising is a very well known example of image decomposition. In such a decomposition, the given image is assumed to be under the influence of noise, and the main purpose is to remove noise without destroying edges. This denoising task can be regarded as a decomposition of the

---

\*An earlier version available as Preprint Number 13-54, Department of Mathematics, Universidade de Coimbra, Portugal.  
<http://www.mat.uc.pt/preprints/ps/p1354.pdf>

<sup>†</sup>Corresponding author. IT, Department of Computer Science, University of Beira Interior, 6201-001, Covilhã, Portugal.  
E-mail: jmoreno@ubi.pt.

<sup>‡</sup>Department of Computer Science, University of Missouri-Columbia, MO 65211 USA. E-mail: prasaths@missouri.edu

<sup>§</sup>Department of Mathematics, University of Coimbra, Portugal

<sup>¶</sup>IT, Department of Computer Science, University of Beira Interior, 6201-001, Covilhã, Portugal.

<sup>||</sup>Department of Computer Science, University of Missouri-Columbia, MO 65211 USA.

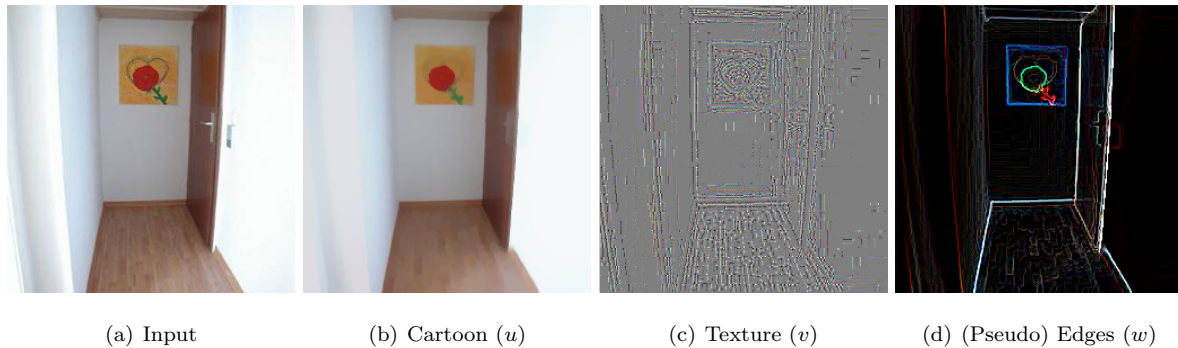


Figure 1: MIT LabelMe decomposition result on an indoor image. Our scheme can obtain piecewise constant cartoon component along with texture and edges for better separation of basic shape elements present in a scene. Better viewed online and zoomed in.

image into noise-free signal and noise part. There exist various methodologies for image restoration, where variational minimization and partial differential equation (PDE) are two of the most popular ones [3].

Another important example of image decomposition is based on its smooth and texture components using the total variation (TV) regularization method. This was first studied by Rudin et al [49] for image restoration. The TV regularization can be written as an unconstrained minimization,

$$\min_u E_{TV}(u) = \int_{\Omega} |\nabla u| \, dx + \frac{1}{2\alpha} \int_{\Omega} |u - f|^2 \, dx. \quad (1)$$

The parameter  $\alpha > 0$  balances the fidelity term with respect to the TV regularization. Let the given image be written as  $f = u + v$ , where the function  $u$  models well structured homogeneous regions (cartoon) and  $v$  defines oscillating patterns such as noise and texture. [34] established the scale connection property of TV for image decomposition, namely that the  $\alpha$  parameter is related to the scale of objects in the image. In particular, Meyer proved that if  $f$  is a characteristic function and is sufficiently small with respect to a norm ( $|f|_* \leq 1/2\alpha$ ), then the minimization of the TV regularization (1) gives  $u = 0$  and  $f = 0$ , which is counter-intuitive since one expects  $u = f$  and  $v = 0$ . Thus, Meyer proposed to use dual of the closure in the bounded variation (BV) space of the Schwartz class for non-trivial solutions, we refer to [34] for more details. This crucial fact has been exploited by [56] to obtain numerical approximations to the Meyer decomposition model, see also related early works [4, 6].

Image denoising methods in general and variational PDE models in particular provide natural decomposition of images, see [3] for a review. Image smoothing and denoising literature is rich in terms of different methodologies utilized and current state of the art techniques [10, 19, 43] have pushed the envelope of optimal improvements [18]. Next we provide a brief overview different approaches utilized in image decomposition.

## 1.1 Literature

While the literature on cartoon and texture decomposition is extensive by now, three lines of inquiries are closely related to the work presented here.

- **Different function spaces for modeling the textures and discrete approximations:** Following Meyer’s seminal work [34], various authors have considered different function spaces to model textures accurately [5, 6, 24, 27, 29, 31, 32, 40, 54].
- **$L^1$  fidelity based TV regularization models:** In another related direction the fidelity term can be made  $L^1$  and is proven to provide contrast preserving restorations. We refer to [16] for the geometric motivation and fine properties of  $L^1$  fidelity term, see also [21]. Applications of  $L^1$ -TV models for cartoon plus texture decomposition are considered as well [2, 22, 27, 37, 58, 59].
- **Different Regularizers instead of TV:** The well-known staircasing property of the TV regularization has been analyzed by many in the past [12, 13, 38] and various modifications have also been studied. To avoid staircasing and blocky restoration results from the classical TV model there have been a variety of methods studied previously. Weighted and adaptive [45–47, 51, 52], nonlocal-TV [30], and higher order [7, 17, 28, 41].

Out of other related decomposition models we mention multi-scale parameter based models [26, 53, 54] which progressively capture texture. Extension to multichannel images in general, RGB images in particular, is also an important area of research [8]. Note that all of the above mentioned methods obtain cartoon and texture decomposition and in this work we obtain edges as part of our scheme. In Figure 1 we show an example decomposition for an indoor image taken from the MIT LabelMe [50] open annotation. Our advanced decomposition provides basic scene elements, since it is based on total variation (edge preserving) smoothing, the cartoon component reflects coarse shapes. This feature is useful in obtaining segmentations and annotations as the edges can provide guideline for separating salient objects [39].

## 1.2 Contributions

In this paper, we propose a new image decomposition scheme which splits a given image into its geometrical and textural part along with an edge capturing diffusion constraint. Following the success of weighted and adaptive TV models, our scheme is based on a weighted TV regularization where the edge-variable-based weight is computed in a data-adaptive way. The scheme is implemented using the splitting method of [9] along with dual minimization scheme for the weighted TV regularization [14]. As a by-product of the implementation via dual minimization we obtain an auxiliary variable which is akin to textural component of the given image. Thus, the scheme studied here provides a cartoon, texture,

edge (CTE) decomposition for digital images, see Figure 2 for some examples<sup>1</sup>.

We consider the color image decomposition using the dual minimization based color TV model. Multi-scale decomposition following the recent work of [54] is also given. Moreover, we provide theoretical analysis of the model with a priori estimates and prove its solvability. Extensive experimental results on synthetic, textured real images are given. Further, illustrative comparison with other state-of-the-art models are undertaken and the results indicate superior performance of our scheme with respect to cartoon, texture separation as well as denoising with edge preservation.

The rest of the paper is organized as follows. Section 2 introduces the adaptive TV regularization coupled with a diffusion PDE. Section 3 provides wellposedness results for our coupled model. In Section 4 we provide the experimental results conducted on real and synthetic images and comparison with related schemes. Finally, Section 5 concludes the paper.

## 2 Diffusion constrained regularization

### 2.1 Weighted total variation minimization

The total variation based regularization [49] given in Eqn. (1) is well-known in edge preserving image restoration, we rewrite it as follows,

$$\min_u E_{TV}^\mu(u) = \int_{\Omega} |\nabla u| \, dx + \mu \int_{\Omega} |u - f|^2 \, dx \quad (2)$$

where now  $\mu > 0$  is the image fidelity parameter which is important in obtaining results in denoising and cartoon+texture decomposition. A related approach is to consider a weighted total variation,

$$\min_u E_{gTV}^\mu(u) = \int_{\Omega} g(x, u, \nabla u) |\nabla u| \, dx + \mu \int_{\Omega} |u - f|^2 \, dx \quad (3)$$

where  $g(x, u, \nabla u)$  represents the generalized weight function. For example, [9] have considered a convex regularization of the variational model

$$\min_u \left\{ \int_{\Omega} g(x) |\nabla u| \, dx + \mu \int_{\Omega} |u - f| \, dx \right\}$$

using a fast minimization based on a dual formulation to get a partition in the geometric and texture information. Note that the image fidelity is changed to  $L^1$  norm, we refer to [16] for more details. The convex regularization version is considered in [9],

$$\min_{u,v} \left\{ \int_{\Omega} g(x) |\nabla u| \, dx + \frac{1}{2\theta} \int_{\Omega} (u + v - f)^2 \, dx + \mu \int_{\Omega} |v| \, dx \right\}, \quad (4)$$

---

<sup>1</sup>We use the words edges or pseudo-edges interchangeably in the text, since the edge component is computed with gradient maps without traditional edge refinement procedures such as maxima suppression [11].





(a) Input ( $f$ )      (b) Cartoon ( $u$ )      (c) Texture  $v$       (d) (Pseudo) Edges ( $w$ )      (e)  $f - (u + v + w)$

Figure 2: The proposed coupled TV regularization with linear diffusion PDE model provides cartoon, texture and edge decomposition of images (stopping parameter  $\epsilon = 10^{-4}$ ). Better viewed online and zoomed in.

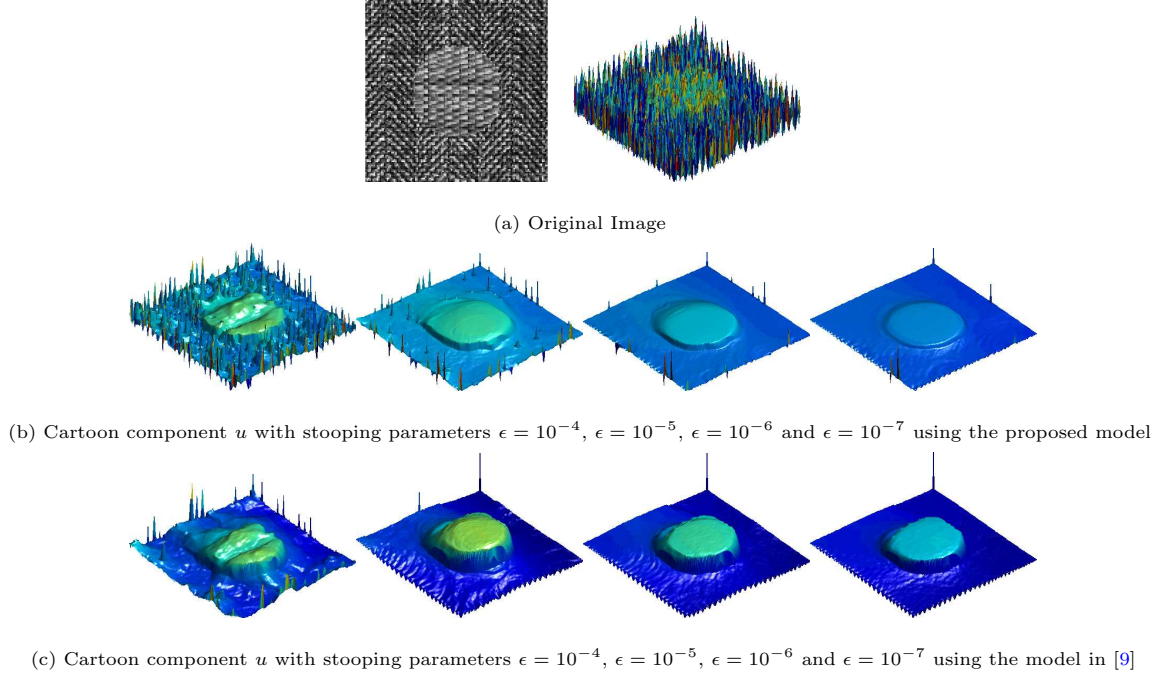


Figure 3: (Color online) Our adaptive diffusion constrained total variation scheme (see Eqn. (9)) with constant  $\mu$ ,  $\lambda$  (second row) provides better edge preserving image decomposition when compared to the traditional TV regularization model (Eqn. (4)) of [9] (third row) as stopping parameters increase from  $\epsilon = 10^{-4}$  to  $\epsilon = 10^{-7}$ . The proposed scheme keeps the structure without diffusing its boundary with the background.

where the parameter  $\theta > 0$  is chosen to be small so that  $f$  almost satisfies  $f \sim u + v$ , with the function  $u$  representing geometric information, *i.e.* the piecewise-smooth regions, and function  $v$  captures texture information lying in the given image. The function  $g$  is an edge indicator function that vanishes at object boundaries, for example,

$$g(x) := \frac{1}{1 + \beta |\nabla f(x)|^2},$$

where  $f$  is the original image and  $\beta$  is an arbitrary positive constant. Thus, we see that TV based minimization models naturally lead to cartoon and texture decomposition of digital images. The image fidelity parameter  $\mu$  can be made data adaptive to obtain texture preserving restorations, see [25].

## 2.2 Description of the model

In our work, we consider the following regularization model which was motivated by a coupled PDE modeling done in [48] for image restoration,

$$\min_u \left\{ \int_{\Omega} \phi(x, u, |\nabla u|) dx + \mu \int_{\Omega} |u - f| dx \right\}, \quad (5)$$

$$\frac{\partial w}{\partial t} = \lambda \operatorname{div}(\nabla w) + (1 - \lambda)(|\nabla u| - w). \quad (6)$$

The choice of regularizer  $\phi$  depends on an application area and among a plethora of convex and non-convex functions available with the classical TV [49] and the non-local TV [30]. Motivated from the above discussions in Section 2.1, and success enjoyed by the weighted  $L^1$ -TV regularization model in image denoising and segmentation, we use  $L^1$ -TV regularizer model as a prime example to illustrate our model here. The proposed CTE model thus consists of a minimization along with a non-homogeneous diffusion equation,

$$\min_u \left\{ \int_{\Omega} g(w) |\nabla u| dx + \int_{\Omega} \mu(x) |u - f| dx \right\}, \quad (7)$$

$$\frac{\partial w}{\partial t} = \lambda(x) \operatorname{div}(\nabla w) + (1 - \lambda(x))(|\nabla u| - w), \quad (8)$$

where  $g(w) = \frac{1}{1+w^2}$ , or  $g(w) = \exp(-w^2)$  (Perona-Malik type diffusion functions [42]), or  $g(w) = |w|^{-1}$ , or  $g(w) = \frac{1}{\sqrt{\epsilon^2 + |w|^2}}$  (total variation diffusion function [49]). That is we solve adaptive data fidelity based weighted total variation minimization for the smooth part  $u$  using Eqn. (7) along with a linear non-homogenous diffusion constraint on  $w$  by solving Eqn. (8). Note that the balancing parameter  $\lambda$  and image fidelity  $\mu$  taking values in  $[0, 1]$  are important in our experimental results. Adaptive ways of choosing these parameters are explained below in Section 2.3. Following [9] we use a splitting with an auxiliary variable  $v$  to obtain

$$\min_{u,v} \left\{ \int_{\Omega} g(w) |\nabla u| dx + \frac{1}{2\theta} \int_{\Omega} (u + v - f)^2 dx + \int_{\Omega} \mu(x) |v| dx \right\}, \quad (9)$$

$$\frac{\partial w}{\partial t} = \lambda(x) \operatorname{div}(\nabla w) + (1 - \lambda(x))(|\nabla u| - w).$$

Thus, the computed solution of these equations provides a representation  $(u, v, w)$ , where the function  $u$  represents the geometric information, the function  $v$  captures the texture information, and the function  $w$  represents the edges lying in the given image. Figure 3 shows a comparison of our scheme ( $\mu = 1$  and  $\lambda = 0.5$ ) and Bresson et al [9] scheme Eqn. (4) for a synthetic texture image which contains two different texture patterns. As can be seen, our scheme (Figure 3(b)) retains the cartoon edges better without diffusing the boundary and the shape is preserved in contrast to Bresson et al's result (Figure 3(c)).

The above coupled system is solved in an alternating iterative way for all the variables  $(u, v, w)$  involved and Chambolle's dual minimization scheme [14] is used for the weighted TV minimization step. We start with the initial conditions

$$(u, v, w)|_{n=0} = (f, \mathbf{0}, \mathbf{1})$$

and use the following steps to compute CTE components:

1. Solving the linear diffusion PDE (8) for  $w$  with  $(u, v)$  fixed:

$$w^{n+1} = w^n + \frac{\delta t}{(\delta x)^2} (\lambda(x) \tilde{\Delta} w^n + (1 - \lambda(x)) (|\nabla u| - w^n)), \quad (10)$$

where  $\delta x$  is spatial discretization step (natural pixel grid),  $\tilde{\Delta}$  is the standard finite difference discretization for the Laplacian and  $\delta t$  is the step size.

2. Solving for the cartoon component  $u$  with  $(v, w)$  fixed:

The minimization problem in  $u$  is given by (see Eqn. (9)),

$$\min_u \left\{ \int_{\Omega} g(w) |\nabla u| dx + \frac{1}{2\theta} \int_{\Omega} (u + v - f)^2 dx \right\}. \quad (11)$$

The solution of (11) is given by

$$u = f - v - \theta \operatorname{div} \mathbf{p}, \quad (12)$$

where  $\mathbf{p} = (p_1, p_2)$  satisfies  $g(w) \nabla(\theta \operatorname{div} \mathbf{p} - (f - v)) - |\nabla(\theta \operatorname{div} \mathbf{p} - (f - v))| \mathbf{p} = 0$ , which is solved using a fixed point method:  $\mathbf{p}^0 = 0$  and

$$\mathbf{p}^{n+1} = \frac{\mathbf{p}^n + \delta t \nabla(\operatorname{div}(\mathbf{p}^n) - (f - v)/\theta)}{1 + \frac{\delta t}{g(w)} |\nabla(\operatorname{div}(\mathbf{p}^n) - (f - v)/\theta)|}.$$

3. Solving for the texture component  $v$  with  $(u, w)$  fixed:

$$\min_v \left\{ \frac{1}{2\theta} \int_{\Omega} (u + v - f)^2 dx + \int_{\Omega} \mu(x) |v| dx \right\}, \quad (13)$$

and the solution is found as

$$v = \begin{cases} f - u - \theta \mu(x) & \text{if } f - u \geq \theta \mu(x), \\ f - u + \theta \mu(x) & \text{if } f - u \leq -\theta \mu(x), \\ 0 & \text{if } |f - u| \leq \theta \mu(x). \end{cases} \quad (14)$$

Next we describe a data adaptive way for choosing the fidelity parameter  $\mu$  using the cartoon component at a previous iteration  $u^n$ .

**Remark 1.** We interchangeably use edges and pseudo-edges as the  $w$  component provides an edge like features from a given image. The definition of edges in a digital image depends on the context and many traditional definitions depend on the magnitude of gradients (i.e.,  $|\nabla I|$ ), hence a solution of the PDE (8) provides a pseudo-edge map, see Figure 2(d).

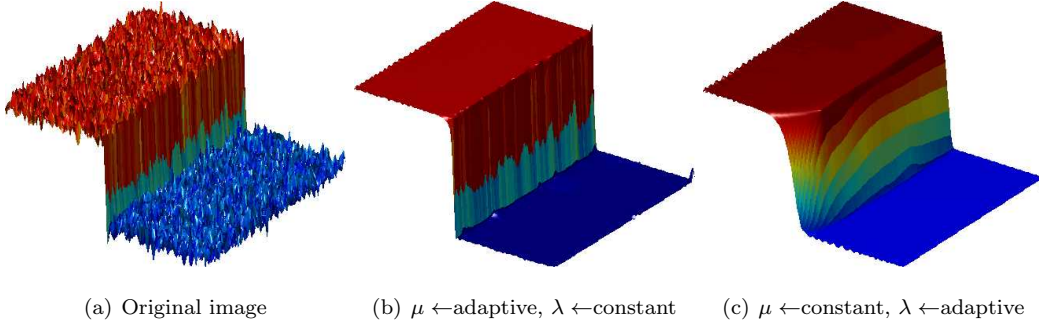


Figure 4: (Color Online) The proposed model (stopping parameter  $\epsilon = 10^{-4}$ ) with adaptive  $\mu_1$  (see Eqn. (17)) and constant  $\lambda (= 1)$  provides better edge preservation in the cartoon component and captures small scale oscillations in the texture component against constant  $\mu (= 1)$  and adaptive  $\lambda$  (using the definition of  $\mu_1$  from Eqn. (17)).

### 2.3 Adaptive fidelity parameter

Here, we consider the data adaptive parameters selection strategies which can provide a balanced approach in obtaining better CTE decomposition results. For the image fidelity parameter  $\mu$  in Eqn. (7) we utilize a local histogram measure which was motivated from the image segmentation model of [36]. For a given gray-scale image  $I : \bar{\Omega} \rightarrow [0, L]$ , let  $\mathcal{N}_{x,r}$  be the local region centered at  $x$  with radius  $r$ . We compute the local histogram of the pixel  $x \in \Omega$  and its corresponding cumulative distribution function

$$P_x(y) = \frac{|\{z \in \mathcal{N}_{x,r} \cap \Omega \mid I(z) = y\}|}{|\mathcal{N}_{x,r} \cap \Omega|} \quad (15)$$

$$F_x(y) = \frac{|\{z \in \mathcal{N}_{x,r} \cap \Omega \mid I(z) \leq y\}|}{|\mathcal{N}_{x,r} \cap \Omega|} \quad (16)$$

for  $0 \leq y \leq L$ , respectively. This allows us to define the following measurable function  $\mu : \Omega \rightarrow \mathbb{R}$ , such that for each  $x \in \Omega$ ,

$$\mu(x) = \mu_1(x) = \frac{\int_0^L F_x(y) dy}{\max_{x \in \Omega} \int_0^L F_x(y) dy}, \quad (17)$$

allowing us to get a weight of how much nonhomogeneous intensity is present in a local region  $\mathcal{N}_{x,r}$  of a given pixel  $x$ . This new feature of the image does not depend on the pixel properties instead provides regional properties, see [36] for more details. Thus, we see that the  $\mu$  is chosen according to local histogram information and is computed in an image adaptive way using the cartoon  $u^n$  in the iterative scheme (13).

We compare our approach with two related adaptive functions:

1. The adaptive formulation of [48] which uses a summation of cartoon components up-to iteration  $n$ .

$$\mu_2(x) = \sum_{i=0}^n G_{\rho_i} \star u^n(x) \quad (18)$$

with  $\rho_i = 1/i^2$  and at  $n = 0$  the  $\lambda_2(x) = 0.05$ .

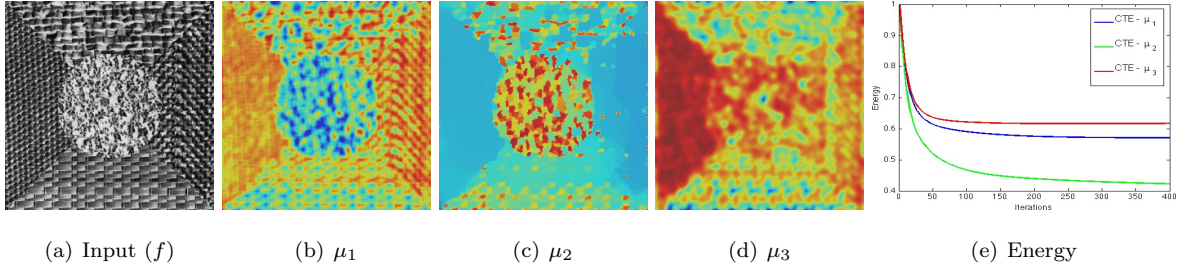


Figure 5: (Color Online) Comparison of different  $\mu$  functions computed using the given input image. (a) Original image. (b)  $\mu_1$  based on local histograms Eqn. (17). (c)  $\mu_2$  based on the work of [48] Eqn. (18). (d)  $\mu_3$  base on the work of [30] Eqn. (19). (e) Energy versus iteration for different adaptive  $\mu$  functions based energy minimization scheme (7-8) with stooping parameter  $\epsilon = 10^{-4}$ .

2. Relative reduction rate based parameter proposed in local TV based scheme [30].

$$\mu_3(x) = \frac{G_\rho \star |\nabla f(x)| - G_\rho \star |L_\sigma \star \nabla f(x)|}{G_\rho \star |\nabla f(x)|}, \quad (19)$$

where  $L_\sigma$  is a low pass filter. Note that this adaptive parameter uses only the initial input image  $f$  whereas the previous choices use  $u$  computed at a previous (Eqn. (17)) or every (Eqn. (18)) iteration.

**Remark 2.** Figure 4 explains the choice of adaptiveness in our coupled model (7-8) for a synthetic image with different texture patterns. The first case with  $\mu$  adaptive,  $\lambda$  constant provides persisting cartoon component whereas the second case with  $\mu$  constant,  $\lambda$  adaptive (same local histogram based measure, Eqn. (17) is used for defining  $\lambda(x)$ ) blurs the boundaries in the final result. Thus, in what follows, we use only  $\mu$  adaptive parameter to illustrate our decomposition results.

Figure 5 shows a comparison of different adaptive  $\mu$  functions for a synthetic texture image. We see that the local histogram based  $\mu_1$  captures the texture components from all the quadrants. Moreover, Figure 5(e) shows that the energy value decreases similarly for different  $\mu$  functions as the iteration increases. Figure 6 shows the usage of different  $\mu$  function when we apply our model (7-8) for the same synthetic image to obtain cartoon ( $u$ ) + texture ( $v$ ) + pseudo-edges ( $w$ ) decomposition. Note that the texture image  $v$  is obtained by linearly transforming its range to  $[0, 255]$  for visualization purposes. Differences outside this range are saturated to 0 and 255 respectively. A similar transformation is applied to the edges ( $w$ ) component as well. Next, we study the wellposedness of the model (7-8) using weak solutions concept and prove some a priori estimates and solvability of the proposed adaptive coupled model.



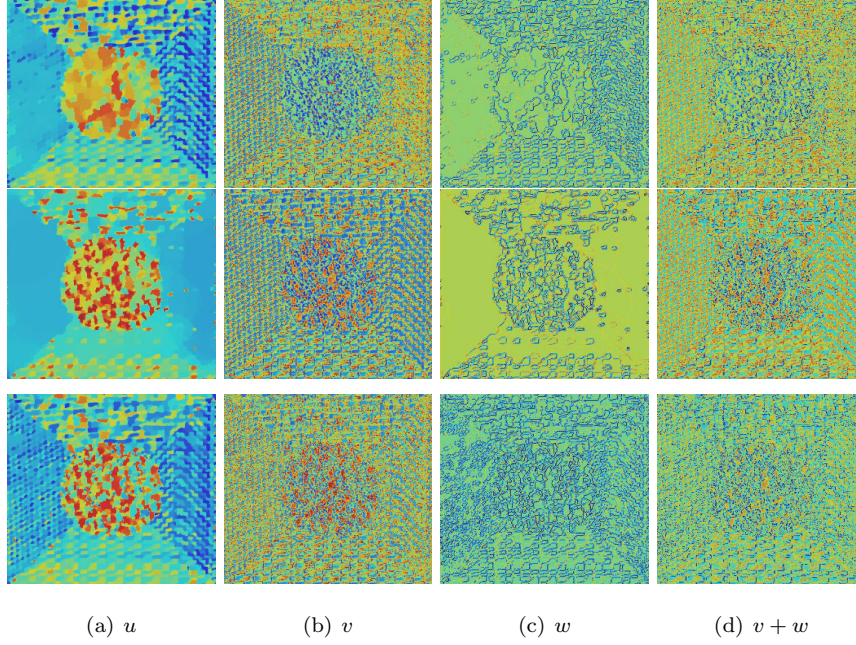


Figure 6: (Color Online) Different  $\mu$  functions based CTE scheme (with  $\lambda$  constant) results (stopping parameter  $\epsilon = 10^{-4}$ ). Top:  $\mu_1$  (local histogram) based result. Middle:  $\mu_2$  result. Bottom:  $\mu_3$  result. (a) Cartoon  $u$ . (b) Texture  $v$ . (c) Pseudo-edges  $w$ . (d)  $v + w$ . Best viewed electronically, zoomed in.

### 3 Wellposedness

#### 3.1 Preliminaries

In the section,  $\Omega$  is considered to be a bounded domain (i.e. an open set in  $\mathbb{R}^2$ ) possessing the *cone property*. We recall that this means that each point  $x \in \Omega$  is a vertex of a *finite cone*  $C_x$  contained in  $\Omega$ , and all these cones  $C_x$  are congruent [1]. Obviously, rectangular domains have this property. Fix also a time interval  $[0, T]$ ,  $T > 0$ .

We study wellposedness of the weighted TV regularization,

$$u(t, x) = \mathbf{u}(x) : \min_{\mathbf{u} : \Omega \rightarrow \mathbb{R}} \left\{ \int_{\Omega} g(w(t, x)) |\nabla \mathbf{u}(x)| dx + \int_{\Omega} \mu(x) |\mathbf{u}(x) - f(x)| dx \right\}, \quad (20)$$

with the diffusion constraint,

$$\frac{\partial w(t, x)}{\partial t} = \Delta_{p, \lambda} w(t, x) + (1 - \lambda(x)) (|\nabla u(t, x)| - w(t, x)), \quad (21)$$

$$w(t, x) = 0, \quad x \in \partial\Omega, \quad (22)$$

$$w(0, x) = F(x), \quad (23)$$

where  $p \geq 2$ , and  $f : \Omega \rightarrow \mathbb{R}$ ,  $F : \Omega \rightarrow [0, +\infty)$ ,  $\lambda : \Omega \rightarrow (0, 1]$ ,  $\mu : \Omega \rightarrow (0, +\infty)$ ,  $g : [0, +\infty) \rightarrow (0, +\infty)$

are prescribed functions. The operator  $\Delta_{p,\lambda}$  is a weighted  $p$ -Laplacian:

$$\Delta_{p,\lambda}v = \lambda \operatorname{div}(|\nabla v|^{p-2}\nabla v) - (1 - |\nabla v|^{p-2})\nabla v \cdot \nabla \lambda. \quad (24)$$

In particular, for  $p = 2$  we recover the linear diffusion case. In this section, for the sake of generality, we admit adaptive  $\lambda$  and generic  $g$ . Note that  $w$  is non-negative by the maximum principle. We consider the Dirichlet boundary condition for  $w$ , but other boundary conditions can also be handled.

We use the brief notations  $L_q$  ( $q \geq 1$ ),  $W_q^m$  ( $m \in \mathbb{R}$ ),  $W_0^{m,q}$  ( $m > 0$ ) for the Lebesgue and Sobolev spaces on  $\Omega$  with values in  $\mathbb{R}$  or  $\mathbb{R}^2$ . Parentheses denote the bilinear form

$$(u, v) = \int_{\Omega} u(x) \cdot v(x) dx.$$

The norm in  $L_2$  is  $\|u\| = \sqrt{(u, u)}$ .

The symbols  $S(\mathcal{J}; E)$ ,  $C(\mathcal{J}; E)$ ,  $L_1(\mathcal{J}; E)$  denote the spaces of Bochner measurable, continuous, Bochner integrable functions on an interval  $\mathcal{J} \subset \mathbb{R}$  with values in a Banach space  $E$ , respectively.

Let  $\mathcal{M}$  be the Banach space of finite Radon measures on  $\Omega$ . It is the dual of the space  $C_0(\Omega)$  (the space of continuous functions on  $\Omega$  that vanish at  $\partial\Omega$ , see e.g. [23]).

Let  $BV$  be the space of functions of bounded variation on  $\Omega$ . For  $v \in BV$ , and  $\phi \in C(\overline{\Omega})$ ,  $\phi \geq 0$ , the *weighted total variation* of  $v$  is

$$TV_{\phi}(v) = \sup_{\psi \in C_0^{\infty}(\Omega): |\psi| \leq \phi} (v, \operatorname{div} \psi). \quad (25)$$

In particular, the *total variation* of  $u$  is

$$TV(v) = TV_1(v). \quad (26)$$

Due to lower semicontinuity of suprema, for every non-negative  $\phi \in C(\overline{\Omega})$  and a weakly-\* converging sequence  $\{v_m\} \subset BV$ , we have

$$TV_{\phi}(v) \leq \lim_{m \rightarrow +\infty} \inf TV_{\phi}(v_m). \quad (27)$$

A more refined argument of the same nature proves

**Lemma 1.** *For any  $\varphi \in S(0, T; C(\overline{\Omega}))$ ,  $\varphi \geq 0$  for a.a.  $t \in (0, T)$ , and a weakly-\* converging sequence  $\{v_m\} \subset L_q(0, T; BV)$ ,  $q > 1$ , one has*

$$TV_{\varphi(t)}(v(t)) \leq \lim_{m \rightarrow +\infty} \inf TV_{\varphi(t)}(v_m(t)) \quad (28)$$

for a.a.  $t \in (0, T)$ .

For  $v \in BV$ ,  $|\nabla v|$  will denote the corresponding total variation measure. The operator

$$|\nabla(\cdot)| : BV \rightarrow \mathcal{M} \quad (29)$$



is bounded. We recall the duality relation

$$TV_\phi(v) = \langle |\nabla v|, \phi \rangle_{\mathcal{M} \times C_0(\Omega)}. \quad (30)$$

The symbol  $C$  will stand for a generic positive constant that can take different values in different lines. We sometimes write  $C(\dots)$  to specify that the constant depends on a certain parameter or value.

We will use the embeddings

$$BV \subset L_q, \quad q \leq 2, \quad (31)$$

$$W_2^1 \subset L_q, \quad q < +\infty, \quad (32)$$

$$W_p^1 \subset C(\overline{\Omega}), \quad p > 2, \quad (33)$$

and

$$\mathcal{M} \subset W_q^{-1}, \quad q < 2, \quad (34)$$

and the Poincaré inequality

$$\|v\|_{W_p^1} \leq C \|\nabla v\|_{L_p}, \quad p \geq 1, \quad v|_{\partial\Omega} = 0. \quad (35)$$

Embeddings (31)–(34) are compact (except for (31) with  $q = 2$ ).

We assume that  $\lambda$ ,  $\nabla \lambda$  and  $g$  are Lipschitz functions,

$$\lambda_0 = \inf_{x \in \Omega} \lambda(x) > 0, \quad g_0 = \sup_{y \geq 0} g(y) < +\infty,$$

and there exists a constant  $C_g$  so that

$$\left| \frac{d(\log g(y))}{dy} \right| \leq \frac{C_g}{1+y} \quad \text{for a.a. } y \geq 0. \quad (36)$$

The last condition means that  $g$  can have at most polynomial decay at infinity.

We assume that  $\mu \in L_\infty(\Omega)$ , and

$$0 < \mu_1 = \operatorname{ess\,inf}_{x \in \Omega} \mu(x) \leq \mu_2 = \operatorname{ess\,sup}_{x \in \Omega} \mu(x) < +\infty.$$

Finally, we assume that

$$F \in L_2, \quad (37)$$

and **at least one** of the following three conditions holds:

$$p > 2, \quad f \in BV, \quad (38)$$

$$p = 2, \quad \exists q > 1 : f \in W_q^1, \quad (39)$$

$$p = 2, \quad f \in BV \cap L_\infty, \quad \exists c_g > 0 : \frac{1}{g(y)} \leq c_g(1+y), \quad y \geq 0. \quad (40)$$

### 3.2 A priori estimates

Before specifying the underlying function spaces and defining the notion of solution, let us derive a formal a priori estimate for problem (20)–(23).

The Euler-Lagrange equation for (20) is

$$-\operatorname{div} \left( g(w) \frac{\nabla u}{|\nabla u|} \right) + \mu \frac{u-f}{|u-f|} = 0, \quad \frac{\partial u / \partial \nu}{|\nabla u|} \Big|_{\partial \Omega} = 0. \quad (41)$$

For each  $t \in [0, T]$ , multiplying (41) by  $\frac{w(u-f)}{g(w)}$ , and integrating over  $\Omega$ , we get

$$\left( g(w) \frac{\nabla u}{|\nabla u|}, \nabla \left( \frac{w(u-f)}{g(w)} \right) \right) + \left( \frac{\mu w}{g(w)}, |u-f| \right) = 0. \quad (42)$$

Thus,

$$\begin{aligned} \left( \frac{\nabla u}{|\nabla u|}, \nabla w(u-f) \right) - \left( \frac{\nabla u}{|\nabla u|}, \frac{g'(w)w}{g(w)} \nabla w(u-f) \right) \\ + (w, |\nabla u|) - \left( w \frac{\nabla u}{|\nabla u|}, \nabla f \right) + \left( \frac{\mu w}{g(w)}, |u-f| \right) = 0. \end{aligned} \quad (43)$$

Multiplying (41) by  $\frac{u-f}{g(w)}$ , and integrating over  $\Omega$ , we find

$$- \left( \frac{\nabla u}{|\nabla u|}, \frac{g'(w)}{g(w)} \nabla w(u-f) \right) + (1, |\nabla u|) - \left( \frac{\nabla u}{|\nabla u|}, \nabla f \right) + \left( \frac{\mu}{g(w)}, |u-f| \right) = 0. \quad (44)$$

Since the last term is non-negative, we conclude that

$$TV(u) \leq TV(f) + C_g \|\nabla w\| \|u-f\|. \quad (45)$$

Multiplying (41) by  $u-f$ , and integrating over  $\Omega$ , we derive

$$(g(w), |\nabla u|) + \|\mu(u-f)\|_{L_1} \leq g_0 TV(f) \quad (46)$$

Multiplying (41) by  $u|u|$ , and integrating over  $\Omega$ , we deduce

$$2(g(w)|u|, |\nabla u|) + \left( \frac{u-f}{|u-f|}, \mu u|u| \right). \quad (47)$$

It is not difficult to obtain the following scalar inequality

$$|a-b|^3 \leq 2(a-b)a|a| + 2b^2|a-b|, \quad a, b \in \mathbb{R}, \quad (48)$$

which enables to conclude from (47) that

$$\|\sqrt{\mu}(u-f)\|^2 + 4(g(w)|u|, |\nabla u|) \leq 2\|\sqrt{\mu}f\|^2. \quad (49)$$

Hence, due to (31),

$$\|u-f\| \leq C(\|f\|) \leq C(\|f\|_{BV}). \quad (50)$$

By (45) and (50),

$$TV(u) \leq C(1 + \|\nabla w\|). \quad (51)$$

Multiplying (21) by  $w$ , and integrating over  $\Omega$ , we get

$$\frac{1}{2} \frac{d\|w\|^2}{dt} + (\lambda, |\nabla w|^p) + ((1-\lambda)w, w) = ((1-\lambda)w, |\nabla u|) - (w \nabla \lambda, \nabla w). \quad (52)$$

Using Hölder's inequality and (36), we deduce from (43) that

$$(w, |\nabla u|) \leq (1 + C_g) \|\nabla w\|_{L_p} \|u - f\|_{L_{p/p-1}} + (w, |\nabla f|). \quad (53)$$

From (52), (53) and Young's inequality we infer

$$\frac{1}{2} \frac{d\|w\|^2}{dt} + \frac{\lambda_0}{2} \|\nabla w\|_{L_p}^p \leq C(g, \lambda_0, p) \|u - f\|_{L_{p/p-1}}^{p/p-1} + C(\lambda, p) \|w\|_{L_{p/p-1}}^{p/p-1} + (w, |\nabla f|). \quad (54)$$

Provided (38) or (39), estimate (50), and embeddings (33) or (32), resp., imply

$$\frac{d\|w\|^2}{dt} + \lambda_0 \|\nabla w\|_{L_p}^p \leq C(1 + \|w\|^{p/p-1} + \|w\|_{W_p^1}). \quad (55)$$

By (35), (37) and usual arguments, (55) yields

$$\|w\|_{L_\infty(0,T;L_2)} + \|w\|_{L_p(0,T;W_0^{1,p})} \leq C. \quad (56)$$

In case (40), we multiply (41) by  $\frac{wu}{g(w)}$ , and integrate over  $\Omega$ , arriving at

$$\begin{aligned} \left( \frac{\nabla u}{|\nabla u|}, u \nabla w \right) - \left( \frac{\nabla u}{|\nabla u|}, u \frac{g'(w)w}{g(w)} \nabla w \right) + (w, |\nabla u|) \\ + \left( \frac{\mu w}{g(w)}, |u - f| \right) + \left( \frac{u - f}{|u - f|}, \frac{\mu w f}{g(w)} \right) = 0. \end{aligned} \quad (57)$$

Then, since the penultimate term is non-negative,

$$\begin{aligned} (w, |\nabla u|) &\leq (1 + C_g) \|\nabla w\| \|u\| + \mu_2 c_g (|f|w, 1 + w) \\ &\leq C(1 + \|\nabla w\| + \|w\|^2). \end{aligned} \quad (58)$$

Now, (52) and (58) yield

$$\frac{d\|w\|^2}{dt} + \lambda_0 \|\nabla w\|_{L_p}^p \leq C(1 + \|w\|^2), \quad (59)$$

which implies (56). In all the three cases, (46), (51) and (56) imply

$$\|u\|_{L_\infty(0,T;L_1)} + \|u\|_{L_p(0,T;BV)} \leq C. \quad (60)$$

The operator

$$\Lambda : BV \rightarrow \mathcal{M},$$

$$\Lambda(v) = (1 - \lambda)|\nabla v|,$$

$$\langle \Lambda(v), \phi \rangle_{\mathcal{M} \times C_0(\Omega)} = \langle |\nabla v|, (1 - \lambda)\phi \rangle_{\mathcal{M} \times C_0(\Omega)},$$

is bounded, so

$$\|(1 - \lambda)|\nabla u|\|_{L_p(0, T; \mathcal{M})} \leq C. \quad (61)$$

The weighted  $p$ -Laplacian operator

$$\Delta_{p, \lambda} : W_0^{1, p} \rightarrow W_{p/p-1}^{-1}$$

is also bounded. Hence, (21), (34), (56) and (61) yield an estimate for the time derivative of  $w$ :

$$\|w'\|_{L_p(0, T; W_q^{-1})} \leq C, \quad q < 2, \frac{q}{q-1} \geq p. \quad (62)$$

### 3.3 Solvability

**Definition 1.** Assume (37) and (38). A pair of functions  $(u, w)$  from the class

$$u \in L_\infty(0, T; L_1) \cap L_p(0, T; BV),$$

$$w \in L_\infty(0, T; L_2) \cap L_p(0, T; W_0^{1, p}) \cap W_p^1(0, T; W_{p/p-1}^{-1}),$$

is called a weak solution to problem (20)–(23) if

$$TV_{g(w(t))}(u(t)) + \|\mu(u(t) - f)\|_{L_1} \leq TV_{g(w(t))}(\mathbf{u}(t)) + \|\mu(\mathbf{u}(t) - f)\|_{L_1}, \quad (63)$$

for any  $\mathbf{u} \in S(0, T; BV)$  and a.a.  $t \in (0, T)$ ,

$$w' - \Delta_{p, \lambda} + (1 - \lambda)w = (1 - \lambda)|\nabla u| \quad (64)$$

in the space  $W_{p/p-1}^{-1}$  for a.a.  $t \in (0, T)$ , and

$$w(0) = F \quad (65)$$

in  $W_{p/p-1}^{-1}$ .

**Remark 3.** This definition is correct since all members of (64) belong to  $W_{p/p-1}^{-1}$  for a.a.  $t \in (0, T)$  (cf. the end of Subsection 3.2), and  $w \in W_p^1(0, T; W_{p/p-1}^{-1}) \subset C([0, T]; W_{p/p-1}^{-1})$ .

**Theorem 1.** Assume (37) and (38). Then there exists a weak solution to (20)–(23).

*Proof.* We can prove the existence of weak solutions via approximation of (20)–(23) by a more regular problem, and consequent passage to the limit (cf. [48, 60]). Let  $(u_m, w_m)$  be a sequence of “approximate” solutions (possibly with “approximate” data  $f_m$  and  $F_m$ ). It essentially suffices to show that (63)–(65) is the limiting case of (20)–(23), i.e., that it is possible to pass to the limit in all the members.

Due to estimates (56), (60), (62), without loss of generality we may suppose that

$$u_m \rightarrow u \text{ weakly} - * \text{ in } L_\infty(0, T; \mathcal{M}), \quad (66)$$

$$u_m \rightarrow u \text{ weakly} - * \text{ in } L_p(0, T; BV), \quad (67)$$

$$w_m \rightarrow w \text{ weakly} - * \text{ in } L_\infty(0, T; L_2), \quad (68)$$

$$w_m \rightarrow w \text{ weakly in } L_p(0, T; W_0^{1,p}), \quad (69)$$

$$w'_m \rightarrow w' \text{ weakly in } L_p(0, T; W_{p/p-1}^{-1}). \quad (70)$$

Note that

$$u \in L_\infty(0, T; L_1) \subset L_\infty(0, T; \mathcal{M}) \cap L_p(0, T; BV). \quad (71)$$

By (33), (34) and the Aubin-Lions-Simon theorem [60],

$$w_m \rightarrow w \text{ strongly in } L_p(0, T; C(\overline{\Omega})), \quad (72)$$

$$w_m \rightarrow w \text{ strongly in } C([0, T]; W_{p/p-1}^{-1}), \quad (73)$$

so

$$w_m(0) \rightarrow w(0) \text{ in } W_{p/p-1}^{-1}, \quad (74)$$

and we can pass to the limit in (65).

Using the representation

$$\|v\|_{L_1} = \sup_{\varphi \in L_\infty, \|\varphi\|_{L_\infty} \leq 1} (\varphi, v), \quad (75)$$

and lower semicontinuity of suprema, we can check that

$$\begin{aligned} \|\mu(u(t) - f)\|_{L_1} &\leq \liminf_{m \rightarrow +\infty} \|\mu(u_m(t) - f)\|_{L_1} \\ &= \liminf_{m \rightarrow +\infty} \|\mu(u_m(t) - f_m)\|_{L_1} \end{aligned} \quad (76)$$

for a.a.  $t \in (0, T)$ . By Lemma 1,

$$TV_{g(w(t))}(u(t)) \leq \liminf_{m \rightarrow +\infty} TV_{g(w(t))}(u_m(t)). \quad (77)$$

But

$$\begin{aligned} &|TV_{g(w_m(t))}(u_m(t)) - TV_{g(w(t))}(u_m(t))| \\ &\leq \|g(w_m(t)) - g(w(t))\|_{L_\infty} TV(u_m(t)) \leq C(g) \|w_m(t) - w(t)\|_{L_\infty} TV(u_m(t)), \end{aligned} \quad (78)$$

so

$$\|TV_{g(w_m)}(u_m) - TV_{g(w)}(u_m)\|_{L_{p/2}(0, T)} \leq C \|w_m - w\|_{L_p(0, T; L_\infty)} \|u_m\|_{L_p(0, T; BV)} \rightarrow 0. \quad (79)$$

Therefore, without loss of generality,

$$TV_{g(w_m(t))}(u_m(t)) - TV_{g(w(t))}(u_m(t)) \rightarrow 0 \quad (80)$$

for a.a.  $t \in (0, T)$ . Due to (76), (77), (80), we can pass to the limit in (63).

On the other hand, (63) with  $u = u_m$ ,  $f = f_m$ ,  $w = w_m$ ,  $\mathbf{u} = u$  gives

$$TV_{g(w_m(t))}(u_m(t)) + \|\mu(u_m(t) - f_m)\|_{L_1} \leq TV_{g(w_m(t))}(u(t)) + \|\mu(u(t) - f_m)\|_{L_1}. \quad (81)$$

Similarly to (78)–(80), we can check that

$$TV_{g(w_m(t))}(u(t)) - TV_{g(w(t))}(u(t)) \rightarrow 0. \quad (82)$$

From (76), (77), (80)–(82) we conclude that

$$TV_{g(w(t))}(u_m(t)) \rightarrow TV_{g(w(t))}(u(t)) \quad (83)$$

for a.a.  $t \in (0, T)$ .

Fix any non-negative function  $\phi \in C_0(\Omega)$ . Let

$$\kappa(t) = \left\| \frac{\phi}{g(w(t))} \right\|_{L_\infty} \quad (84)$$

and

$$\varphi(t) = \kappa(t)g(w(t)) - \phi. \quad (85)$$

For a.a.  $t \in (0, T)$ ,  $\varphi(t)$  is a non-negative continuous function on  $\overline{\Omega}$ . By Lemma 1 and (83), we infer that

$$\begin{aligned} TV_\phi(u(t)) &= \kappa(t)TV_{g(w(t))}(u(t)) - TV_{\varphi(t)}(u(t)) \geq \lim_{m \rightarrow +\infty} \sup(\kappa(t)TV_{g(w(t))}(u_m(t)) - TV_{\varphi(t)}(u_m(t))) \\ &= \lim_{m \rightarrow +\infty} \sup TV_\phi(u_m(t)). \end{aligned} \quad (86)$$

But, due to (28),

$$TV_\phi(u(t)) \leq \lim_{m \rightarrow +\infty} \inf TV_\phi(u_m(t)). \quad (87)$$

Thus,

$$TV_\phi(u(t)) = \lim_{m \rightarrow +\infty} TV_\phi(u_m(t)), \quad (88)$$

for every non-negative  $\phi \in C_0(\Omega)$ , which yields

$$|\nabla u_m(t)| \rightarrow |\nabla u(t)| \quad (89)$$

weakly-\* in  $\mathcal{M}$  for a.a.  $t \in (0, T)$ . Then (34) implies

$$(1 - \lambda)|\nabla u_m(t)| \rightarrow (1 - \lambda)|\nabla u(t)| \quad (90)$$

strongly in  $W_{p/p-1}^{-1}$  for a.a.  $t \in (0, T)$ . Due to (67) and (34),

$$\|(1-\lambda)|\nabla u_m|\|_{L_p(0,T;W_{p/p-1}^{-1})} \leq C. \quad (91)$$

By (90), (91) and [35, Proposition 2.8, Remark 2.10],

$$(1-\lambda)|\nabla u_m| \rightarrow (1-\lambda)|\nabla u| \text{ strongly in } L_q(0,T;W_{p/p-1}^{-1}), \quad \forall q < p. \quad (92)$$

Rewrite (64) as

$$w' + Aw = K(u, w), \quad (93)$$

where

$$A(w) = -\operatorname{div}(\lambda|\nabla w|^{p-2}\nabla w) + (1-\lambda)w, \quad K(u, w) = -\nabla w \cdot \nabla \lambda + (1-\lambda)|\nabla u|. \quad (94)$$

It is easy to see that the operator  $A : W_0^{1,p} \rightarrow W_{p/p-1}^{-1}$  is monotone, coercive and hemi-continuous (cf. [33]). By (72) and (92),

$$K(u_m, w_m) \rightarrow K(u, w) \text{ strongly in } L_{p/p-1}(0, T; W_{p/p-1}^{-1}).$$

Hence, we can successfully pass to the limit in (93) via Minty-Browder monotonicity technique (cf. [33]).  $\square$

**Definition 2.** Assume (37) and (39) or (40). A pair of functions  $(u, w)$  from the class

$$u \in L_\infty(0, T; L_1) \cap L_2(0, T; BV), \quad (95)$$

$$w \in L_\infty(0, T; L_2) \cap L_2(0, T; W_0^{1,2}) \cap W_2^1(0, T; W_q^{-1}), \quad \forall q < 2, \quad (96)$$

is called a pseudosolution to problem (20)–(23) if there is a sequence  $(u_m, w_m, p_m)$  such that each pair  $(u_m, w_m)$  is a weak solution to (20)–(23) with  $p = p_m$ ,

$$u_m \rightarrow u \text{ weakly} - * \text{ in } L_\infty(0, T; \mathcal{M}),$$

$$u_m \rightarrow u \text{ weakly} - * \text{ in } L_2(0, T; BV),$$

$$w_m \rightarrow w \text{ weakly} - * \text{ in } L_\infty(0, T; L_2),$$

$$w_m \rightarrow w \text{ weakly in } L_2(0, T; W_0^{1,2}),$$

$$w_m \rightarrow w \text{ strongly in } L_2(0, T; L_q), \quad \forall q < +\infty,$$

$$w_m \rightarrow w \text{ strongly in } C([0, T]; W_q^{-1}), \quad \forall q < 2,$$

$$w'_m \rightarrow w' \text{ weakly in } L_2(0, T; W_q^{-1}), \quad \forall q < 2,$$

$$p_m \rightarrow 2.$$

**Theorem 2.** Assume (37) and (39) or (40). Then there exists a pseudosolution to (20)–(23).

*Proof.* The proof is based on estimates (56), (60), (62) and the proof of Theorem 1.  $\square$

## 4 Experimental Results

### 4.1 Implementation details

The proposed scheme is implemented using the dual minimization [14] for the weighted TV (Eqn. (7)) and explicit Euler finite difference scheme for the non-homogenous linear diffusion (Eqn. (8)). The edge indicator function  $g(w) = 1/(1 + w^2)$  is used for all the results reported here. We obtained similar results for other  $g$  functions. The adaptive  $\mu_1$  based results are reported here unless otherwise stated explicitly and  $\mu_2$  provided similar results whereas  $\mu_3$  provided slightly blurred cartoon components, see Section 2.3 for details. The parameters  $\delta x = 1$ ,  $\delta t = 1/8$  and  $\theta = 10^{-2}$  are fixed, and the best results according to the  $\max(|u^{n+1} - u^n|, |v^{n+1} - v^n| \leq \epsilon)$  are shown. By constant  $\lambda$  and  $\mu$  in the results we mean they are taken as constant value 0.5 and 1 respectively. The implementation of the proposed scheme is done for the constant choice ( $\mu \leftarrow \text{constant}$ ,  $\lambda \leftarrow \text{constant}$ ), the adaptive choice ( $\mu \leftarrow \text{adaptive}$ ,  $\mu \leftarrow \text{constant}$ ) and the multiscale case ( $\mu \leftarrow \text{multiscale}$ ,  $\lambda \leftarrow \text{constant}$ ).

The algorithm is visualized in MATLAB 7.8(R2009a) on a 64-bit Windows 7 laptop with 3GB RAM, 2.20GHz CPU. It takes on average  $< 10$  sec for 50 iterations for 3 channels image of size  $481 \times 321$ . Implementation is done over the following databases: Brodatz texture collection<sup>2</sup>, Mosaic art images<sup>3</sup>, Kodak Lossless True Color Image Suite<sup>4</sup>, Color Test Images Database<sup>5</sup>, USC-SIPI Image Database<sup>6</sup> and Simulated Brain Database<sup>7</sup>, Berkeley segmentation dataset of 500<sup>8</sup>.

### 4.2 Image decomposition results

#### 4.2.1 Gray-scale images

We first show decomposition results of [9] with our model in Figure 7 for a synthetic image which consists of two different texture regions. Comparing the cartoon - texture decomposition of our scheme (Figure 7(b)) with the results of Bresson et al (Figure 7(c)), we see that they behave different visually. For example, the shape of the diamond at the center is preserved well in our scheme whereas the [9] scheme blurs it in the final result. Figure 7(c) shows the energy value against number of iterations for the same synthetic image, which indicates that our adaptive CTE scheme decreases the energy values comparable to [9] model. More grayscale image decomposition results are given in Figure 2. We see that the cartoon component obtained are piecewise constant segments indicating the potential for image

---

<sup>2</sup><http://multibandtexture.recherche.usherbrooke.ca>

<sup>3</sup><http://www.cse.cuhk.edu.hk/leojia/projects/texturesep/>

<sup>4</sup><http://r0k.us/graphics/kodak>

<sup>5</sup><http://www.hlevkin.com/TestImages/classic.htm>

<sup>6</sup><http://sipi.usc.edu>

<sup>7</sup><http://brainweb.bic.mni.mcgill.ca/brainweb/>

<sup>8</sup><http://www.eecs.berkeley.edu/Research/Projects/CS/vision/bsds/>



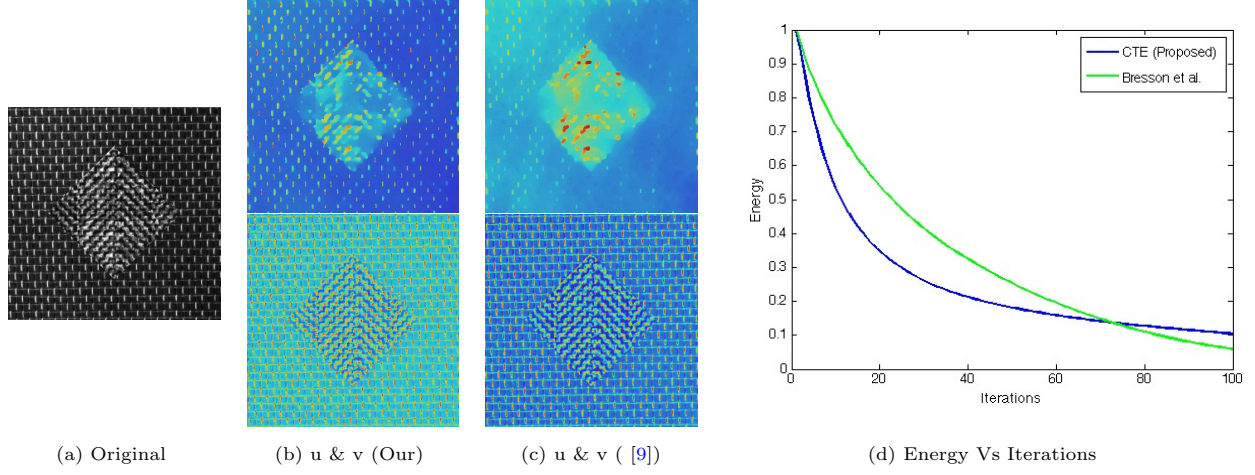


Figure 7: (Color online) Comparison of our constant  $\mu, \lambda$  proposed scheme (second column) with Bresson et al [9] (third column), shows that our scheme preserves large-scale textures and shape boundaries (stopping parameter  $\epsilon = 10^{-4}$ ). Energy value comparison between our scheme CTE and Bresson et al. [9] shows similar convergence property. Best viewed electronically, zoomed in.

segmentation [44]. The texture and edges component are complementary and it is clear that edges are based on the cartoon subregions, see for example, Figure 2(d) top row.

#### 4.2.2 Color images

We further provide image decomposition for color images [8, 22] by using vectorial TV version in Eqn. (7) following [8]. We consider the following vectorial TV with non-homogenous diffusion equation:

$$\min_{\mathbf{u}=(u_1, u_2, u_3)} \left\{ \int_{\Omega} g(w_i) \sqrt{\sum_{i=1}^3 |\nabla u_i|^2} dx + \sum_{i=1}^3 \int_{\Omega} \mu(x) |u_i - f_i| dx \right\},$$

$$\frac{\partial w_i}{\partial t} = \lambda_i(x) \operatorname{div}(\nabla w_i) + (1 - \lambda_i(x))(|\nabla u_i| - w_i),$$

where each scalar function  $u_i : \Omega \rightarrow \mathbb{R}$ ,  $1 \leq i \leq 3$  represent one component of the RGB color system. Note that following our alternating iterative scheme given by equations (10), (12) and (14) the new solutions  $(u_i, v_i, w_i)$  are given by:

$$u_i = f_i - v_i - \theta \operatorname{div} \mathbf{p}_i, \quad (97)$$

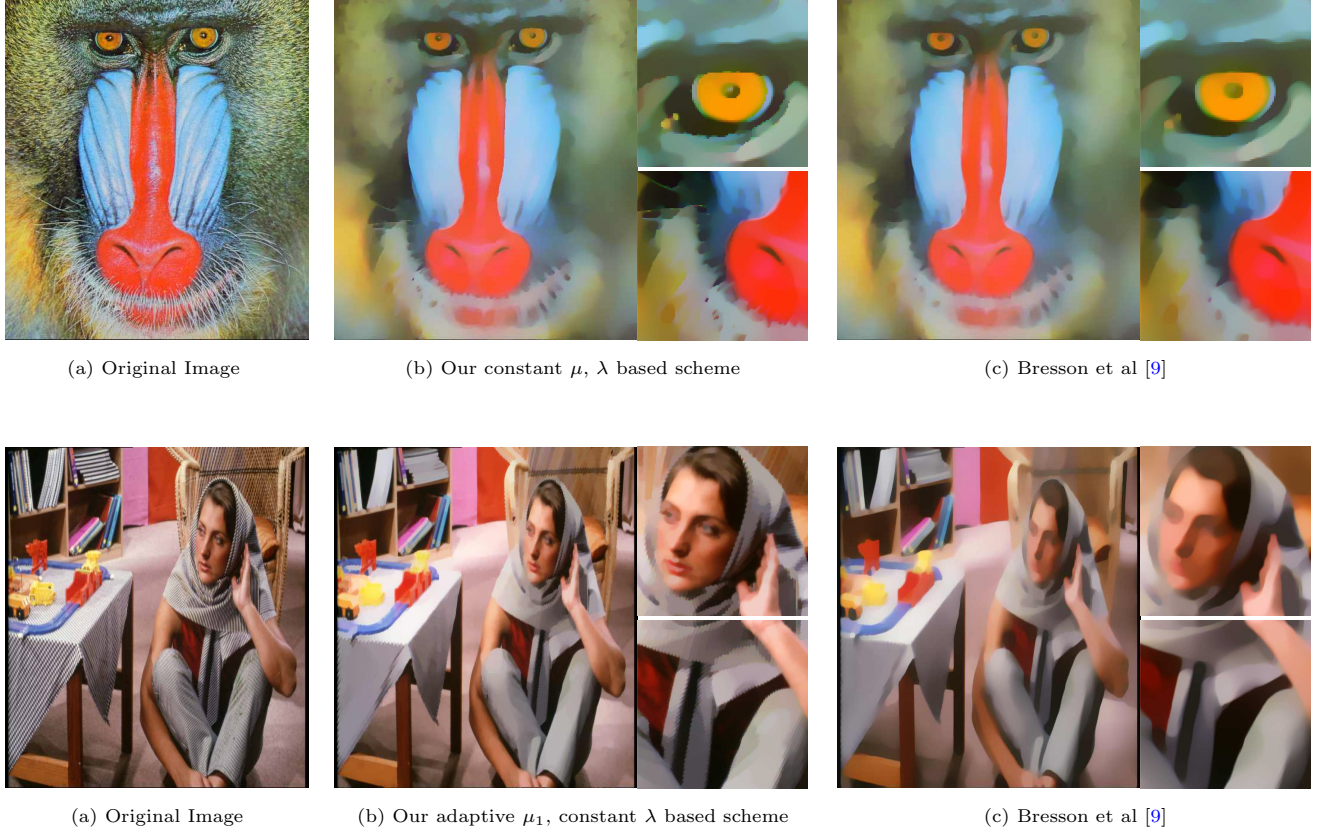


Figure 8: (Color online) Our diffusion constrained total variation scheme (stopping parameter  $\epsilon = 10^{-4}$ ) provides better edge preserving cartoon component  $u$  when compared to the traditional TV regularization model [9]. Even with constant  $\mu, \lambda$  the proposed scheme provides better results (see top row (b)). The crop regions highlight that the proposed scheme provides better preservation of large scale textures compared to [9] model. Best viewed electronically, zoomed in.

where  $\mathbf{p}_i = (p_{i_1}, p_{i_2})$  satisfies  $g(w_i)\nabla(\theta \operatorname{div} \mathbf{p}_i - (f_i - v_i)) - |\nabla(\theta \operatorname{div} \mathbf{p}_i - (f_i - v_i))|\mathbf{p}_i = 0$ , which is solved using a fixed point method:  $\mathbf{p}_i^0 = 0$  and

$$\mathbf{p}_i^{n+1} = \frac{\mathbf{p}_i^n + \delta t \nabla(\operatorname{div}(\mathbf{p}_i^n) - (f_i - v_i)/\theta)}{1 + \frac{\delta t}{g(w_i)} \sqrt{\sum_{i=1}^3 |\nabla(\operatorname{div}(\mathbf{p}_i^n) - (f_i - v_i)/\theta)|^2}}.$$

$$v_i = \begin{cases} f_i - u_i - \theta\mu(x) & \text{if } f_i - u_i \geq \theta\mu(x), \\ f_i - u_i + \theta\mu(x) & \text{if } f_i - u_i \leq -\theta\mu(x), \\ 0 & \text{if } |f_i - u_i| \leq \theta\mu(x). \end{cases} \quad (98)$$

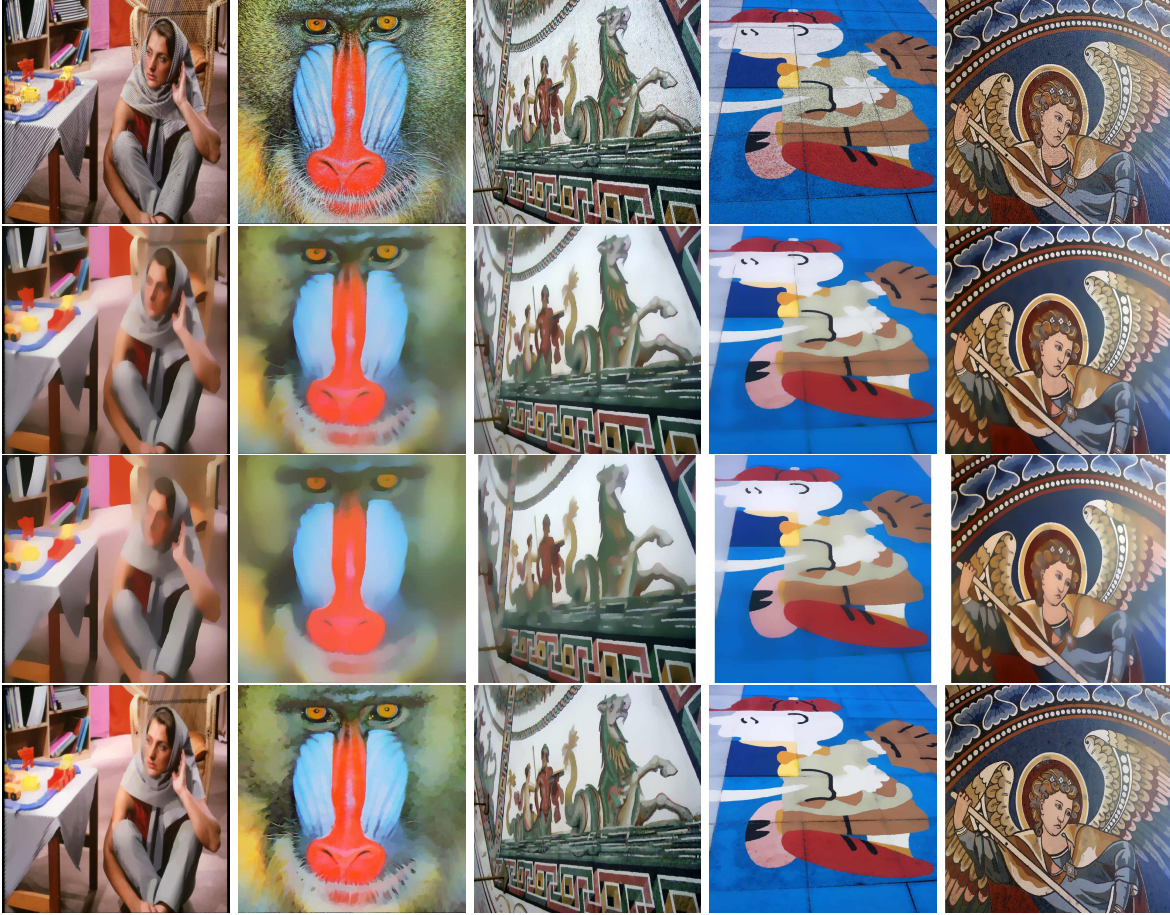


Figure 9: (Color online) Effect of constant  $\mu$  in color image decomposition using our coupled scheme on the cartoon ( $u$ ) component. First row: Original color RGB images. Cartoon component result for constant  $\mu$ ,  $\lambda$  with stopping parameter, Second row:  $\epsilon = 10^{-4}$ , and Third row:  $\epsilon = 10^{-6}$ . As can be seen decreasing the stopping parameter removes more texture details and provides piecewise constant cartoon image. Last row: Shows the proposed scheme results with adaptive  $\mu_1$ , see Eqn. (17) and constant  $\lambda$  (stopping parameter  $\epsilon = 10^{-4}$ ) . Best viewed electronically, zoomed in.



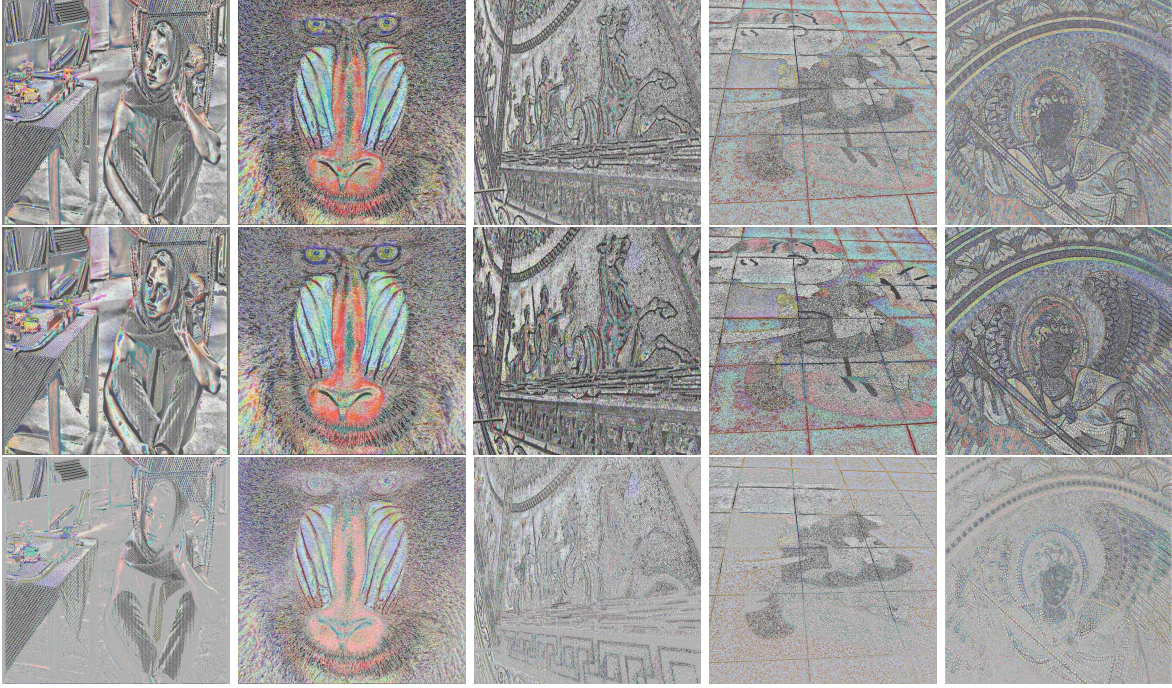


Figure 10: (Color online) Corresponding texture components  $v$ . Arrangement is as in Figure 9. Best viewed electronically, zoomed in.



Figure 11: (Color online) Corresponding edge functions  $w$ . Arrangement is as in Figure 9. Best viewed electronically, zoomed in.

$$w_i^{n+1} = w_i^n + \frac{\delta t}{(\delta x)^2} (\lambda(x) \tilde{\Delta} w_i^n + (1 - \lambda(x)) (|\nabla u_i| - w_i^n)). \quad (99)$$

Figure 8 shows the cartoon components of our CTE scheme with constant and adaptive  $\mu_1$  against the traditional TV based scheme of [9] for two standard RGB test images. As can be seen, our scheme obtains better edge preserving cartoon ( $u$ ) components. The close-up shots indicate that our scheme also avoids blurring of edges, see for example *Barbara* face. See also Figure 3 where the proposed scheme with adaptive  $\mu_1$  provides better shape preservation as stopping parameters increase from  $\epsilon = 10^{-4}$  to  $\epsilon = 10^{-7}$ . Next, Figures 9-11 shows decomposition for a variety of RGB images for two different iteration values in our proposed CTE scheme with constant  $\mu$  against adaptive  $\mu_1$  based results. As can be seen in Figure 9, increasing the number of iterations removes more texture details and provides piecewise constant (smoother) cartoon images. Our adaptive  $\mu_1$  based scheme results (last row) on the other hand keep most of the salient edges. This can be seen further in Figure 10 (last row) where the adaptive  $\mu_1$  based scheme captures only small scale oscillations corresponding to texture components whereas the constant  $\mu$  based results remove strong edges as well. Figure 11 show the corresponding edge functions, and it can be seen that adaptive scheme has more information than in constant parameter case. Thus, we conclude that, using adaptive  $\mu$  provides an image adaptive way of obtaining edge preserving cartoon components without sacrificing overall decomposition properties.

Figure 12 shows the cartoon component of two different color images as well as the edge functions given by the proposed model, and Canny edge maps [11] computed in all the three channels<sup>9</sup>. As observed the function  $w$  captures edges based on the cartoon subregions *i.e.* large intensity gradients while the Canny edge maps captures large and small intensity gradients.

#### 4.2.3 Comparison with other decomposition methods

Next we use the grayscale digitize images from USC-SIPI Image Database to compare the performance of the CTE model together with the adaptive and multi-scale case with the following schemes: TV- $H^{-1}$  decomposition model (OSV, using finite differences) [40], TV- $G_p$  decomposition model (VC, finite differences channel-wise) [55], TV-*Garbor* decomposition model (AGO, Chambolle's projection algorithm) [6],  $BV^2 - L^2$  model (BP, which uses an algorithm close to the one set by dual minimization of [14] and [55]) [7],  $TV - L^1$  model (CP, a first-order primal-dual algorithm) [15],  $L^r$ -TV scheme for color images (DHC, using a unified Moreau-Yosida based primal-dual approach) [20], and the NL- Means algorithm (BCM, a improvement of the classical and state-of-the-art methods in image denosing) [10] which computes the local average color of the most resembling pixels using non-local means.

Numerical results are given in Table 1 for sixteen standard natural grayscale images of size  $256 \times$

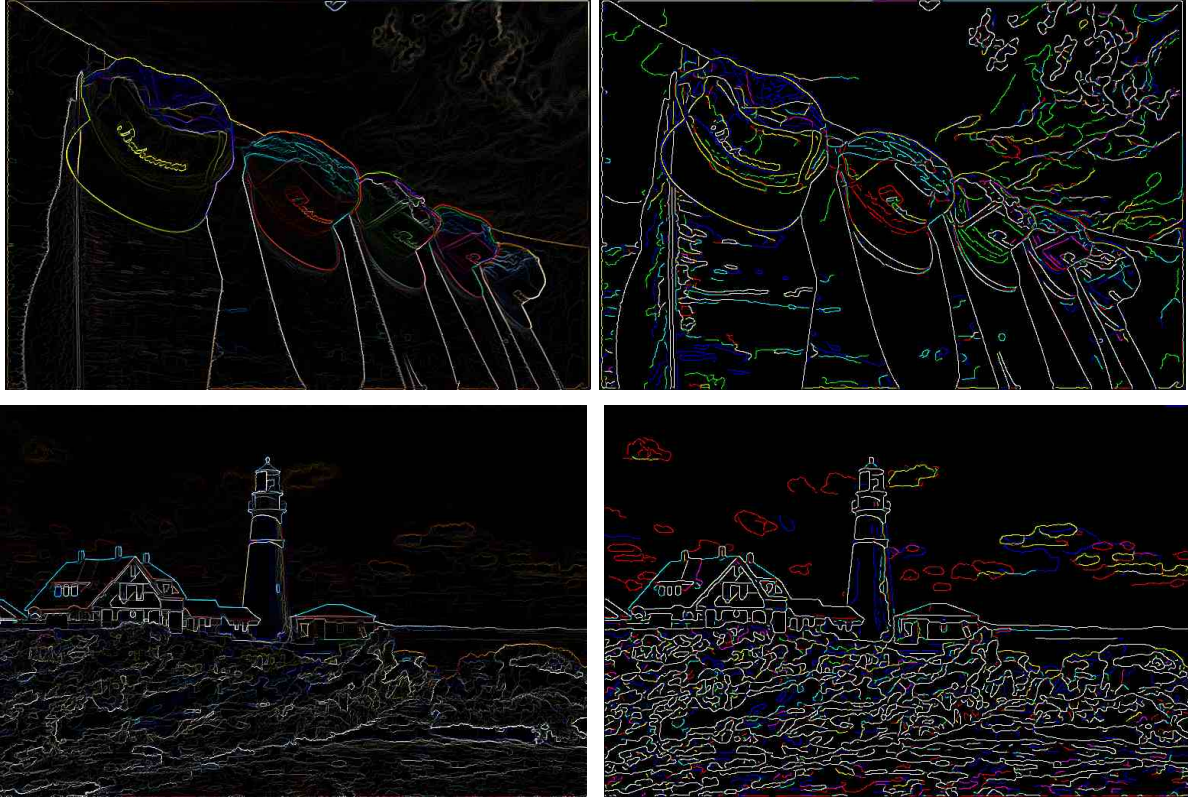
---

<sup>9</sup>Computed using the MATLAB's default command `edge(u, 'canny')`.





(a) Input ( $f$ ) and  $u$  components using the proposed model



(b) (Pseudo) Edges ( $w$ )

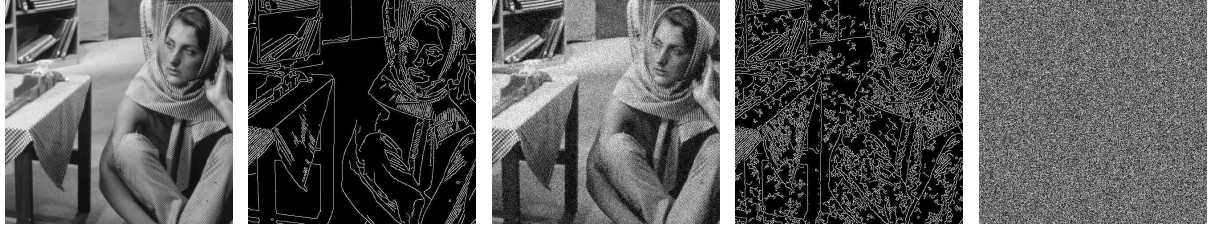
(c) Canny Edges

Figure 12: (Color online) Pseudo edge maps & Canny Edges. First Row: Input ( $f$ ) and  $u$  components using the proposed model with ( $\mu \leftarrow$  adaptive,  $\lambda \leftarrow$  constant) and stopping parameter  $\epsilon = 10^{-4}$ . Second and Third Row: (Pseudo) Edges ( $w$ ) (First Column) and Canny Edges (Second Column).

Image/MSSIM	OSV	VC	AGO	BP	CP	DHC	BCM	MCTE	ACTE	CCTE
Girl1†/0.2081	27.5748	28.1667	28.0247	27.1771	27.9446	28.3862	28.4113	<b>28.8536</b>	28.3557	<u>28.8266</u>
	0.7664	0.7669	0.7705	0.7531	0.7604	0.7732	0.7293	<b>0.7971</b>	0.7893	<u>0.7939</u>
Couple1‡/0.2029	27.1529	28.3845	27.7122	27.4384	27.8213	28.1447	28.5528	<u>28.5297</u>	28.0973	<b>29.4769</b>
	0.6918	0.7080	0.7022	0.7063	0.7042	0.7283	0.7045	<u>0.7467</u>	0.7439	<b>0.7548</b>
Girl2‡/0.1482	29.6239	30.6253	29.6591	30.6260	29.7908	32.0758	30.9228	<b>32.2619</b>	30.7951	<u>32.1304</u>
	0.8730	0.8039	0.8829	0.8779	0.8751	<u>0.8950</u>	0.7991	<b>0.8964</b>	0.8933	0.8821
Girl3‡/0.2261	29.4733	29.3198	28.8185	28.2566	28.7244	30.6547	29.3895	<b>31.3260</b>	29.1061	<u>31.1257</u>
	0.8470	0.8029	0.8335	0.8092	0.8145	0.8014	0.7831	<u>0.8469</u>	<b>0.8595</b>	0.8379
House1†/0.2297	27.1664	26.5337	27.7950	27.4868	28.0119	29.2988	<u>29.4386</u>	29.0679	28.4171	<b>29.5162</b>
	0.7858	0.7626	0.7831	0.7950	0.7795	0.7993	0.7603	<b>0.8138</b>	<u>0.8090</u>	0.8064
Tree†/0.3959	23.7801	24.4972	24.0548	24.2811	24.3028	26.3365	26.0382	<u>26.9758</u>	24.3702	<b>27.0157</b>
	0.7259	0.7549	0.7231	0.7487	0.7314	0.7654	<u>0.7684</u>	<b>0.7702</b>	0.7489	0.7666
Jelly1†/0.1700	29.7350	29.8272	29.4804	30.0963	29.2544	30.6860	30.2663	<b>31.4578</b>	<u>31.2529</u>	30.9478
	0.9181	0.8297	0.9351	0.9153	0.9178	0.9360	0.8407	<u>0.9369</u>	<b>0.9376</b>	0.9145
Jelly2†/0.2294	28.8000	28.9457	27.5507	28.1674	27.9968	29.1260	29.2134	<b>30.0485</b>	29.5462	<u>29.9156</u>
	0.9098	0.8385	0.9029	0.8923	0.9005	0.8227	0.8443	<b>0.9202</b>	<u>0.9182</u>	0.9020
Splash‡/0.4151	30.6488	28.9810	29.9935	31.4922	31.2080	<u>33.1049</u>	31.0800	<b>33.8236</b>	31.3856	31.2644
	0.8825	0.8312	0.8891	0.8818	0.8740	0.8669	0.8732	<u>0.8975</u>	0.8935	<b>0.9020</b>
Tiffany‡/0.4482	29.2555	28.0636	28.6905	30.2667	29.7630	31.2730	29.6920	<b>32.0779</b>	30.7028	<u>31.3727</u>
	0.8617	0.8254	0.8534	0.8425	0.8491	0.8567	0.8628	<b>0.8708</b>	0.8612	<u>0.8685</u>
Mandrill‡/0.7097	20.4765	21.6728	20.7883	21.9056	20.9060	23.7888	<b>23.9897</b>	<u>23.7899</u>	20.8689	22.3085
	0.65255	0.7651	0.6443	0.6962	0.6530	0.8002	<b>0.8247</b>	<u>0.8117</u>	0.6520	0.7713

Table 1: PSNR (dB) and MSSIM comparison of various decomposition schemes with noise level  $\sigma = 30$  for standard test images from the USC-SIPI database with size  $\dagger = 256 \times 256$  (Noisy PSNR = 22.11) and  $\ddagger = 512 \times 512$  (Noisy PSNR = 22.09). Each row indicates PSNR/MSSIM values for different test images. The diffusion with multiscale ( $\mu \leftarrow$  multiscale,  $\lambda \leftarrow$  constant), adaptive choice ( $\mu \leftarrow$  adaptive,  $\lambda \leftarrow$  constant) and constant CTE scheme ( $\mu \leftarrow$  constant,  $\lambda \leftarrow$  constant) are given as MCTE, ACTE and CCTE (last three columns) respectively (stopping parameter  $\epsilon = 10^{-4}$ ). Compared methods are OSV [40], VC [55], AGO [6], BP [7], CP [15], DHC [20], BCM [10]. Best results are indicated in boldface and the second best is underlined.

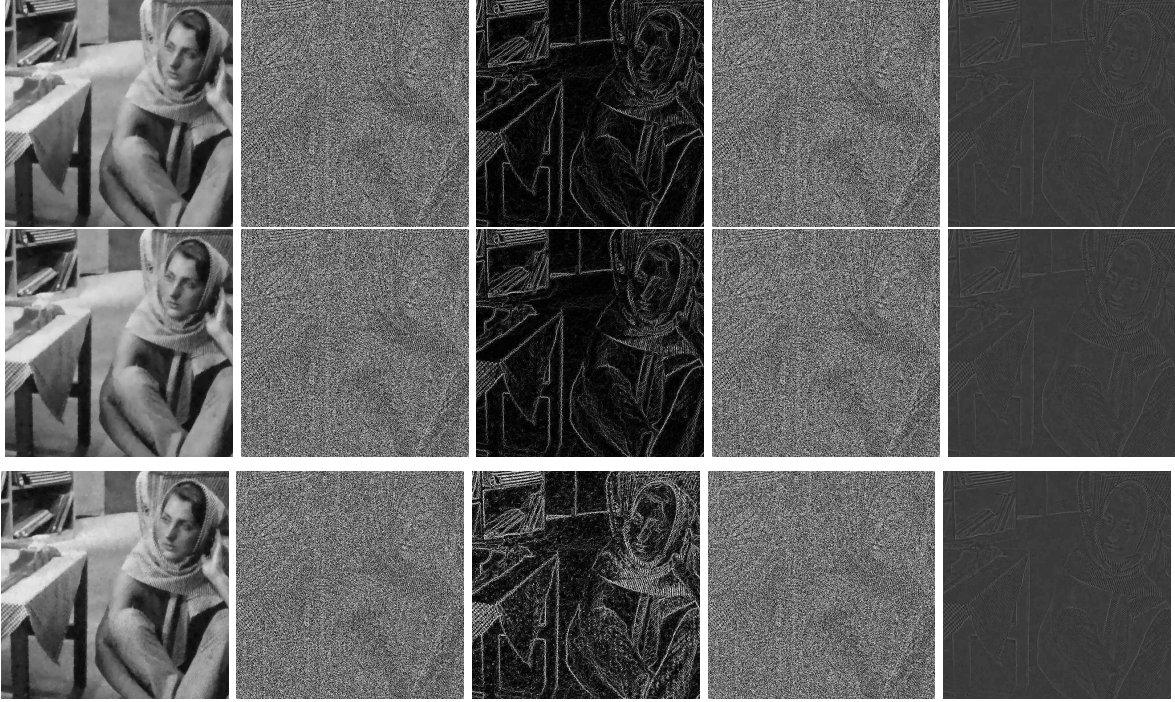




(a) *Barbara* image (b) Canny edges (c) Noisy *Barbara* (d) Canny edges (e) Input noise



(b)  $u$  &  $f - u$  for VC [55] (c)  $u$  &  $f - u$  for OSV [40] (d)  $u$  &  $f - u$  for AGO [6]



(e)  $u, v, w, f - u$ , and  $f - (u + v + w)$  components for the proposed scheme.

Figure 13: Decomposition of noise inputs. (a) *House*, *F-16* and *Barbara* images corrupted by Gaussian noise images (standard deviation  $\sigma = 30$ ). (b)-(d)  $u$  &  $f - u$  components provided by the VC [55], OSV [40] and AGO [6] schemes, respectively. (e)  $u, v, w, f - u$  and  $f - (u + v + w)$  components using the proposed CTE scheme with (CTE -  $\mu \leftarrow$  constant,  $\lambda \leftarrow$  constant) for the Third row, with (ACTE -  $\mu \leftarrow$  adaptive,  $\lambda \leftarrow$  constant) for the Fourth row and (MCTE -  $\mu \leftarrow$  multiscale,  $\lambda \leftarrow$ ) for the Fifth row. The corresponding PSNR (dB) and MSSIM measures for each model are displayed in Table 1.



256 and  $512 \times 512$ . As we can see the proposed scheme based on multi-scale lambda ( $\mu \leftarrow$ multiscale,  $\lambda \leftarrow$ constant) and the adaptive choice ( $\mu \leftarrow$ multiscale,  $\lambda \leftarrow$ constant) performs well for a variety of images. Even with the adaptive choice (ACTE,  $\mu \leftarrow$ adaptive,  $\lambda \leftarrow$ constant) outperforms previous variational models bases  $H^{-1}$ ,  $G_p$  and *Garbor* norms and in some cases the  $L^r$ -TV and the NL-Means schemes. For textured images such as *Mandrill* and *Barbara* we perform all variational models except the NL-means algorithm. We remark that the proposed CTE model does not aim to give state-of-the-art results for image denoising, and instead concentrates on demonstrating how our decomposition model can be harnessed for noise removal and edge detection. Figure 13 shows decomposition for *Barbara* into different components for some of the schemes in Table 1. We note that for other schemes we are able to decompose the image in  $u$  (smooth) and  $f - u$  (random noise). In our case, we are able to obtain edge variable  $w$  component. We also notice that for our model the random noise component  $f - u$  is directly given by the  $v$  component.

## 4.3 Image denoising results

### 4.3.1 Error metrics

Currently there are no quantitative ways to evaluate different decomposition algorithms. In particular which smooth, texture and edge separation model are better is an open research question in image quality assessment. The proposed decomposition provides piecewise cartoon component which is obtained using a weighted TV regularization in an edge preserving way, see Figure 9 (last row). Hence, as a byproduct we obtain image denoising, with  $u$  the denoised image and  $v + w$  the ‘noise’ part. To compare the schemes quantitatively for the purpose of denoising, we utilize two commonly used error metrics in the image denoising literature, one is the classical peak signal to noise ratio (PSNR) [3], and the other one is the mean structural similarity measure (MSSIM) [57].

1. PSNR is given in decibels ( $dB$ ). A difference of  $0.5 dB$  can be identified visually. Higher PSNR value indicates optimum denoising capability.

$$\text{PSNR}(u) := 20 * \log 10 \left( \frac{u_{max}}{\sqrt{MSE}} \right) dB, \quad (100)$$

where  $MSE = (mn)^{-1} \sum \sum (u - u_0)$ ,  $m \times n$  denotes the image size,  $u_{max}$  denotes the maximum value, for example in 8-bit images  $u_{max} = 255$ .

2. MSSIM index is in the range  $[0, 1]$ . The MSSIM value near one implies the optimal denoising capability of the scheme [57] and is mean value of the SSIM metric. The SSIM is calculated between two windows  $\omega_1$  and  $\omega_2$  of common size  $N \times N$ ,

$$\text{SSIM}(\omega_1, \omega_2) = \frac{(2\mu_{\omega_1}\mu_{\omega_2} + c_1)(2\sigma_{\omega_1\omega_2} + c_2)}{(\mu_{\omega_1}^2 + \mu_{\omega_2}^2 + c_1)(\sigma_{\omega_1}^2 + \sigma_{\omega_2}^2 + c_2)},$$

Method	$\mu \leftarrow \text{constant}$ $\lambda \leftarrow \text{adaptive}$	$\mu \leftarrow \text{adaptive}$ $\lambda \leftarrow \text{constant}$	Figure Example	Noise Level	Stopping Parameter	Convergence Time(s)	PSNR (dB)/MSSIM
CTE (Proposed)		✓	14 (b)	$\sigma = 20$	$\epsilon = 10^{-4}$	30.47	28.7938/0.7723
			14 (c)	$\sigma = 20$	$\epsilon = 10^{-6}$	38.71	27.3510/0.7147
			15 (b)	$\sigma = 30$	$\epsilon = 10^{-6}$	38.61	26.5238/0.6774
CTE (Proposed)	✓		14 (d)	$\sigma = 20$	$\epsilon = 10^{-4}$	30.96	28.2464/0.7237
			14 (e)	$\sigma = 20$	$\epsilon = 10^{-6}$	32.20	26.1983/0.6796
			15 (c)	$\sigma = 30$	$\epsilon = 10^{-6}$	32.33	26.7451/0.6792
[48]	✓		14 (f)	$\sigma = 20$	$\epsilon = 10^{-4}$	5.07	27.3646/0.7178
			14 (g)	$\sigma = 20$	$\epsilon = 10^{-6}$	40.57	25.4476/0.6970
			15 (d)	$\sigma = 30$	$\epsilon = 10^{-6}$	40.30	25.0559/0.6543

Table 2: Image denoising error metrics (average) comparison using original coupled PDE scheme [48] for different noise levels and parameters on the Berkeley segmentation dataset (BSDS) 500. Some examples corresponding to the entries are shown above in Figure 14 and Figure 15.

where  $\mu_{\omega_i}$  the average of  $\omega_i$ ,  $\sigma_{\omega_i}^2$  the variance of  $\omega_i$ ,  $\sigma_{\omega_1\omega_2}$  the covariance,  $c_1, c_2$  stabilization parameters, see [57] for more details.

**Remark 4.** Note that the SSIM is a better error metric than PSNR as it provides a quantitative way of measuring the structural similarity of denoised image against the original noise-free image. To adapt PSNR and SSIM error metrics to color images one can convert the color image into gray<sup>10</sup> and then compute PSNR and MSSIM error metrics for the converted gray-scale image. In this paper, in order to compare with the scheme on [48], we compute the PSNR and MSSIM on each channel and use the average as a final value.

#### 4.3.2 Comparison with the previous model

Table 2 compares proposed scheme with that of [48] using the both PSNR (dB) and MSSIM error metrics average for Berkeley segmentation dataset (BSDS) images. We implemented both the schemes on the full Berkeley segmentation dataset of 500 noisy images for two different noise levels and obtained similar improvements. Figures 14-15 show some example images corresponding to Table 2. As can be seen from the zoomed in versions, the proposed CTE scheme provides cleaner cartoon components (denoised images, see Figures 14(b-e)-15(b,c)) in contrast to original coupled PDE model [48] which either excessively blurs out details (Figure 14(f,g)) or keeps noisy regions (Figure 15(d)) in final results.

#### 4.3.3 Comparison of adaptive fidelity parameters

Figure 16 gives a comparison for the implementation of our CTE model ( $\mu \leftarrow \text{adaptive}$ ,  $\lambda \leftarrow \text{constant}$ ) by using adaptive fidelity parameters  $\mu_1$  (proposed),  $\mu_2$  (based on the work of [48]) and  $\mu_3$  (studied

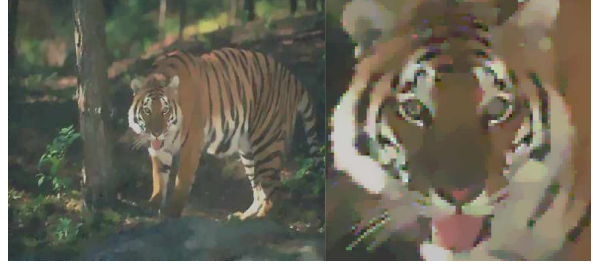
<sup>10</sup>For example, using MATLAB’s command `rgb2gray`.



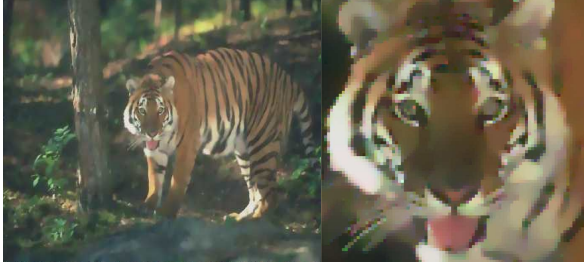
(a) Input noise ( $\sigma = 20$ ), (PSNR, MSSIM) = (24.1759, 0.5130)



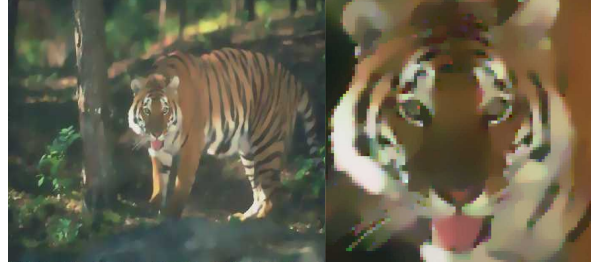
(b) Proposed ( $\mu \leftarrow \text{adaptive}$ ,  $\lambda \leftarrow \text{constant}$ )  
(PSNR, MSSIM) = (28.6484, 0.7675)



(c) Proposed ( $\mu \leftarrow \text{adaptive}$ ,  $\lambda \leftarrow \text{constant}$ )  
(PSNR, MSSIM) = (27.5146, 0.6993)



(d) Proposed ( $\mu \leftarrow \text{constant}$ ,  $\lambda \leftarrow \text{adaptive}$ )  
(PSNR, MSSIM) = (27.6574, 0.7285)



(e) Proposed ( $\mu \leftarrow \text{constant}$ ,  $\lambda \leftarrow \text{adaptive}$ )  
(PSNR, MSSIM) = (26.8005, 0.6849)



(f) [48] (Adaptive)  
(PSNR, MSSIM) = (26.1172, 0.7540)



(g) [48] (Adaptive)  
(PSNR, MSSIM) = (24.8883, 0.7057)

Figure 14: (Color online) Better edge preserving image restoration results were obtained using our scheme in comparison with the original coupled PDE model [48]. The stopping parameters were chosen according to maximum MSSIM values, see Table 2 for the corresponding values.



Figure 15: (Color online) Better edge preserving image restoration results were obtained using our scheme in comparison with the original coupled PDE model [48]. The stopping parameters were chosen according to maximum MSSIM values, see Table 2 for the corresponding values.

in [30]) for a close-up *flower* image corrupted with Gaussian noise level  $\sigma = 20$ . As shown different decomposition levels based on smooth + random noise + edges components are given according to the adaptive parameter  $\mu$ . In terms of PSNR and MSSIM error metrics the  $\mu_1$  choice improves better the denoising result. Note the similar convergence property of the energy value between our  $\mu_1$  choice and the  $\mu_3$  adaptive parameter.

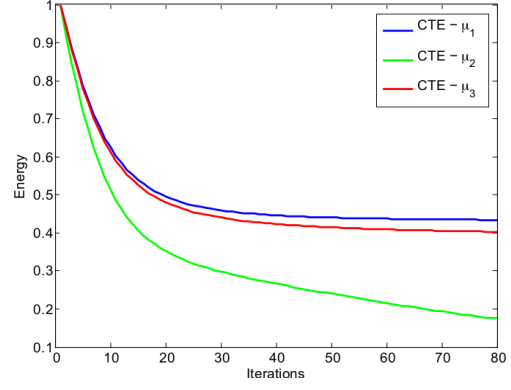
#### 4.3.4 Brain MRI image decomposition

Figure 17 shows input Brain MR images from the Simulated Brain Database and its corresponding  $(u, v, w)$  functions for slices 50, 70 and 120 together with their corresponding inputs. Lack of sharp edges in the denoised Brain MRI images (Third-Fourth rows) can be attributed to the spatial relaxation based for the coupling PDE scheme. Spatial smoothing based regularization introduces a slight blur on each edge map  $w$  (Fifth row). Although, we gradually reduce the smoothing results by varying the stopping



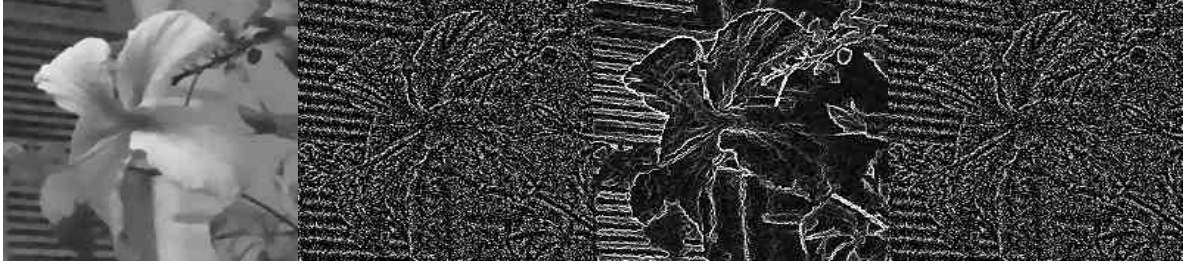


(a) Input noise ( $\sigma = 20$ )



(b) Energy vs Iteration for different  $\mu$  choices

(c)  $u, v, w, f - u$  components for our proposed scheme using  $\mu_1$  with (PSNR, MSSIM) = (27.6623, 0.8143)



(d)  $u, v, w, f - u$  components for our proposed scheme using  $\mu_2$  with (PSNR, MSSIM) = (24.6084, 0.6823)



(e)  $u, v, w, f - u$  components for our proposed scheme using  $\mu_3$  with (PSNR, MSSIM) = (25.6414, 0.7503)

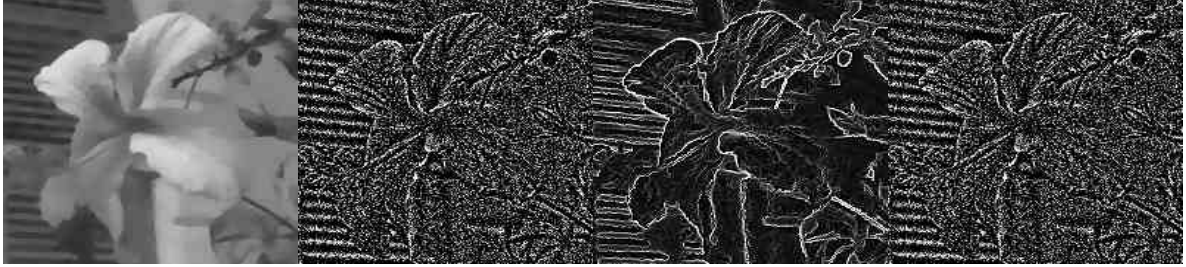
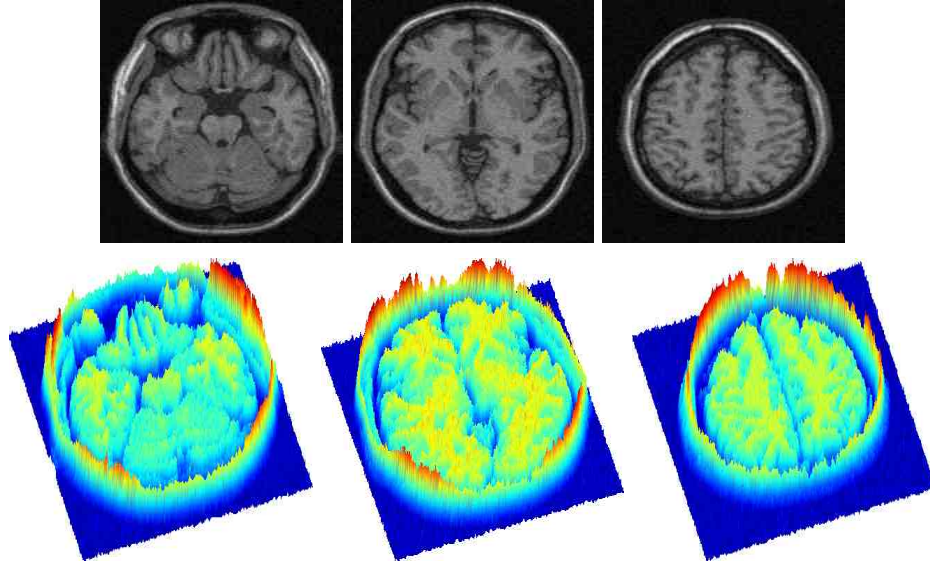
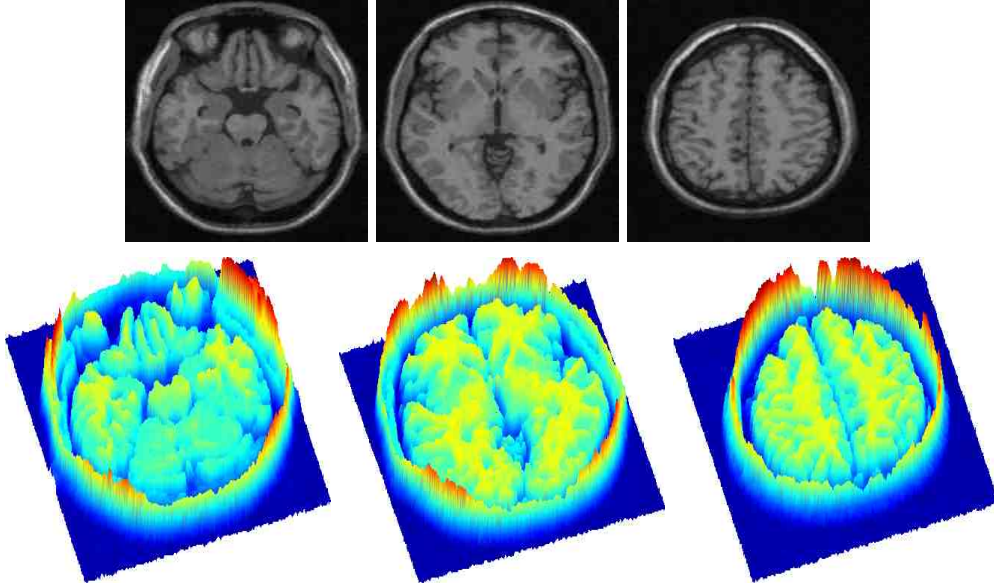


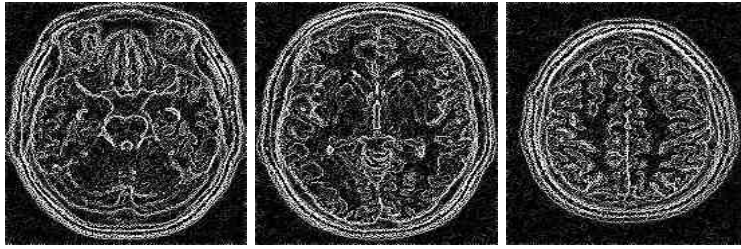
Figure 16: Comparison of different  $\mu$  functions computed using a real image corrupted with Gaussian noise level  $\sigma = 20$  and stopping parameter  $\epsilon = 10^{-4}$ . (a) Original image. (b) Energy versus iteration for different adaptive  $\mu$  functions based energy minimization scheme (7-8). (c)  $\mu_1$  based on local histograms Eqn. (17). (d)  $\mu_2$  based on the work of [48] Eqn. (18). (e)  $\mu_3$  base on the work of [30] Eqn. (19).



(a) Noisy brain MRI images



(b) Cartoon components ( $u$ )



(c) Edges components ( $w$ )

Figure 17: (Color online)  $u$  &  $w$  components using our proposed model with ( $\mu \leftarrow$  adaptive,  $\lambda \leftarrow$  constant) and stopping parameter  $\epsilon = 10^{-4}$  for different Brain MR images (slice: 50, 70 and 120 respectively).

parameter  $\epsilon$  the strong discontinuities are preserved well and noise is removed effectively within regions.

#### 4.4 Multi-scale decomposition

Following [54] we can make the weighted TV model with multi-scale parameter  $\lambda$ . Note that this is slightly different from the original multi scale usage in [53], here we use it in the constraint Eqn. (8). Let us briefly recall the model proposed in [54] where the texture component  $v$  is modeled using  $G_p$  norm. That is, the minimization is carried out for both  $u, v$ ,

$$\inf_{u,v} \left\{ E(f, \lambda; u, v) = |u|_{BV(\Omega)} + \mu \|f - u - v\|_{L^2(\Omega)}^2 + \lambda \|v\|_{G_p(\Omega)} \right\},$$

with  $G_p$  consisting of all distributions which can be written as,

$$v = \partial_x g_1 + \partial_y g_2 = \text{div}(\vec{g}), \quad \vec{g} \in L^p(\Omega, \mathbb{R}^2).$$

The  $G_p$  norm is defined as,

$$\|v\|_{G_p(\Omega)} = \inf \left\{ \|\vec{g}\|_{L^p(\Omega)} \mid v = \text{div}(\vec{g}), \vec{g} \in L^p(\Omega, \mathbb{R}^2) \right\}.$$

We utilize the same modeling for the texture component  $v$  in our splitting step of the proposed weighted TV model (see Eqn. (4)),

$$\min_{u,v} \left\{ \int_{\Omega} |\nabla u| dx + \mu \|f - u - v\|_{L^2(\Omega)}^2 + \lambda \|v\|_{G_p(\Omega)} \right\} \quad (101)$$

Finally, we compare multiscale version (101) with the multi-scale TV decomposition results of [54]. Figure 18 shows the comparison result on a synthetic image for 5 steps and our scheme retains the cartoon component clearly than the Tang and He [54]. Moreover, the texture components show a progressive capture of small scale oscillations.

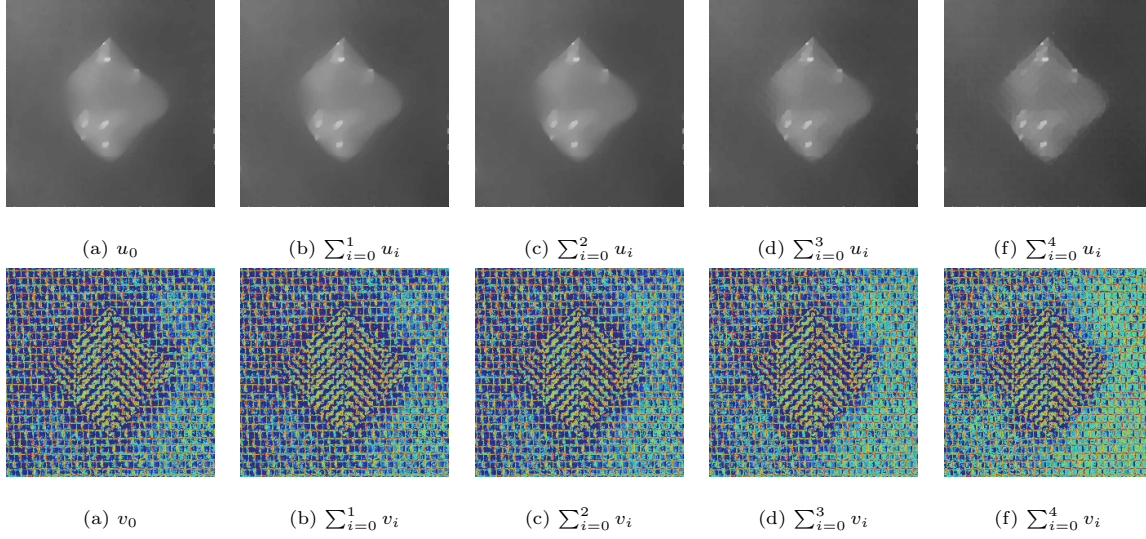
## 5 Conclusion

We have presented a new image decomposition model coupling a variational and PDE via a weighted total variation regularization algorithm (CTE model). Our main contribution is twofold:

- 1) The proposed decomposition model gets an image decomposition into its cartoon, texture and edge components with fixed, adaptive and multcale parameters for the  $L^1$ -fitting term by utilizing a local histogram along with a diffusion equation. Extensive experiments using a fast dual minimization based splitting implementation indicates that the proposed scheme is useful for edge preserving image decomposition on real and noisy images. Comparative results indicate the proposed scheme is useful in denoising natural images as well in multi scale image decomposition.



Multiscale cartoon and texture extraction using our proposed CTE method



Multiscale cartoon and texture extraction using the hierarchical decomposition of Tang and He [54]

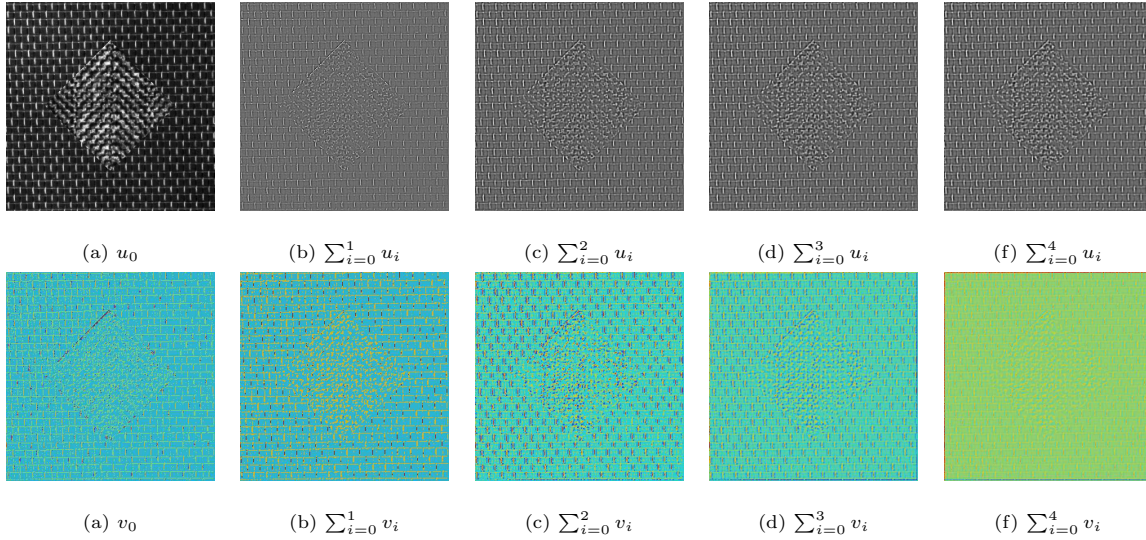


Figure 18: (Color online) Multiscale cartoon and texture decomposition of a synthetic image for 5 steps by implementing our proposed approach (top two rows) (stopping parameter  $\epsilon = 10^{-4}$ ) and the hierarchical method from [54] (bottom two rows).



- 2) We fashioned a new well posed scheme to transform the non-linear problem to a set of subproblems that are much easier to solve quickly via an optimization technique and a linear diffusion PDE solution.

It is well known that there is no unique decomposition of an image into three scales: cartoon, texture and edges. At close range, texture and edges may be just a set of well-structured objects that can be kept in the cartoon part or the textural part according to a scale (equivalently iteration) parameter. We proposed an adaptive choice computed on local windows based histogram information as well as a multi-scale adaptation weight parameter for the  $L^1$ -fitting term, allowing us to get satisfactory results. There are other adaptive parameter choices for constructing a general decomposition model and we believe the proposed method is general in the sense that other regularizers (instead of TV) can be utilized in computing the cartoon component. We also remark that our denoising results are proof-of-concept for the proposed CTE model and we do not claim it outperforms state-of-the-art methods such as the nonlocal means [10] or BM3D [19] which are specifically designed for optimal denoising results.

## References

- [1] R. Adams. *Sobolev spaces*. Academic Press, New York, NY, USA, 1975. Pure and Applied Mathematics, Vol. 65.
- [2] P. Athavale and E. Tadmor. Integro-differential equations based on  $(BV, L^1)$  image decomposition. *SIAM Journal on Imaging Sciences*, 4(1):300–312, 2011.
- [3] G. Aubert and P. Kornprobst. *Mathematical problems in image processing: Partial differential equation and calculus of variations*. Springer-Verlag, New York, USA, 2006.
- [4] J.-F. Aujol, G. Aubert, L. Blanc-Féraud, and A. Chambolle. Image decomposition into a bounded variation component and a oscillating component. *Journal of Mathematical Imaging and Vision*, 22(1):71–88, 2005.
- [5] J.-F. Aujol and A. Chambolle. Dual norms and image decomposition models. *International Journal of Computer Vision*, 63(1):85–104, 2005.
- [6] J.-F. Aujol, G. Gilboa, T. Chan, and S. Osher. Structure-texture image decomposition – modeling, algorithms and parameter selection. *International Journal of Computer Vision*, 67(1):111–136, 2006.
- [7] M. Bergounioux and L. Piffet. A second-order model for image denoising. *Set-Valued and Variational Analysis*, 18(3-4):277–306, 2010.

- [8] X. Bresson and T. F. Chan. Fast dual minimization of the vectorial total variation norm and applications to color image processing. *Inverse Problem and Imaging*, 2(4):455–484, 2008.
- [9] X. Bresson, S. Esedoglu, P. Vanderghelynst, J. Thiran, and S. Osher. Fast global minimization of the active contour/snake model. *Journal of Mathematical Imaging and Vision*, 28(2):151–167, 2007.
- [10] A. Buades, B. Coll, and J. M. Morel. A review of image denoising methods, with a new one. *Multiscale Modeling and Simulation*, 4(2):490–530, 2006.
- [11] J. F. Canny. A computational approach to edge detection. *IEEE Transactions on Pattern Analysis and Machine Intelligence*, 8(6):679–698, 1986.
- [12] V. Caselles, A. Chambolle, D. Cremers, M. Novaga, and T. Pock. An introduction to total variation in image analysis. In *Theoretical Foundations and Numerical Methods for Sparse Recovery (Ed. M. Fornasier)*, volume 9 of *Radon Series on Computational and Applied Mathematics*, pages 263–340. De Gruyter, 2010.
- [13] V. Caselles, A. Chambolle, and M. Novaga. Total variation in imaging. In *Handbook of Mathematical Methods in Imaging (Ed. O. Scherzer)*, pages 1016–1057. Springer, 2011.
- [14] A. Chambolle. An algorithm for total variation minimization and applications. *Journal of Mathematical Imaging and Vision*, 20(1–2):89–97, 2004.
- [15] A. Chambolle and T. Pock. A first-order primal-dual algorithm for convex problems with applications to imaging. *Journal of Mathematical Imaging and Vision*, 40(1):120–145, 2011.
- [16] T. F. Chan and S. Esedoglu. Aspects of total variation regularized L1 function approximation. *SIAM Journal on Applied Mathematics*, 65(5):1817–1837, 2005.
- [17] T. F. Chan, A. Marquina, and P. Mulet. High-order total variation-based image restoration. *SIAM Journal on Scientific Computing*, 22(2):503–516, 2000.
- [18] P. Chatterjee and P. Milanfar. Is denoising dead? *IEEE Transactions on Image Processing*, 19(4):895–911, 2010.
- [19] K. Dabov, A. Foi, V. Katkovnik, and K. Egiazarian. Image denoising by sparse 3D transform-domain collaborative filtering. *IEEE Transactions on Image Processing*, 16(8):2080–2095, 2007.
- [20] Y. Dong, M. Hintermuller, and M. M. Rincon-Camacho. A multi-scale vectorial  $L^\tau$ -TV framework for color image restoration. *International Journal of Computer Vision*, 92(3):296–307, 2011.
- [21] V. Duval, J.-F. Aujol, and Y. Gousseau. The TVL1 model: A geometric point of view. *Multiscale Modeling and Simulation*, 8(1):154–189, 2009.

- [22] V. Duval, J.-F. Aujol, and L. Vese. Mathematical modeling of textures: application to color image decomposition with a projected gradient algorithm. *Journal of Mathematical Imaging and Vision*, 37(3):232–248, 2010.
- [23] I. Fonseca and G. Leoni. *Modern methods in the calculus of variations:  $L^p$  spaces*. Springer Monographs in Mathematics. Springer, New York, 2007.
- [24] J. Garnett, T. Le, Y. Meyer, and L. Vese. Image decomposition using bounded variation minimization and generalized homogeneous Besov spaces. *Applied and Computational Harmonic Analysis*, 23(1):25–56, 2007.
- [25] G. Gilboa, N. Sochen, and Y. Y. Zeevi. Variational denoising of partly textured images by spatially varying constraints. *IEEE Transactions on Image Processing*, 15(8):2281–2289, 2006.
- [26] J. Gilles. Multiscale texture separation. *Multiscale Modelling and Simulation*, 10(4):1409–1427, 2012.
- [27] A. Haddad. Texture separation  $BV - G$  and  $BV - L^1$  models. *Multiscale Modelling and Simulation*, 6(1):273–286, 2007.
- [28] Y. Hu and M. Jacob. Higher degree total variation (hdtv) regularization for image recovery. *IEEE Transactions on Image Processing*, 21(5):2559–2571, 2012.
- [29] T. Le, L. Lieu, and L. Vese.  $(\Phi, \Phi^*)$  image decomposition and minimization algorithms. *Journal of Mathematical Imaging and Vision*, 33(2):135–148, 2009.
- [30] T. Le, J.-M. Morel, and L. Vese. Fast cartoon + texture image filters. *IEEE Transactions on Image Processing*, 19(8):1978–1986, 2010.
- [31] T. Le and L. Vese. Image decomposition using total variation and  $\text{div}(\text{BMO})$ . *Multiscale Modeling and Simulation*, 4(2):390–423, 2005.
- [32] L. Lieu and L. Vese. Image restoration and decomposition via bounded total variation and negative Hilbert Sobolev spaces. *Applied Mathematics and Optimization*, 58(2):167–193, 2008.
- [33] J.-L. Lions. *Quelques méthodes de résolution des problèmes aux limites non linéaires*. Dunod, 1969.
- [34] Y. Meyer. *Oscillating Patterns in Image Processing and Nonlinear Evolution Equations*. American Mathematical Society, Boston, MA, USA, 2001. The Fifteenth Dean Jacqueline B. Lewis Memorial Lectures, Vol. 22 of University Lecture Series.
- [35] D. R. Moreira and E. V. Teixeira. On the behavior of weak convergence under nonlinearities and applications. *Proc. Amer. Math. Soc.*, 133(6):1647–1656 (electronic), 2005.

- [36] K. Ni, X. Bresson, T. Chan, and S. Esedoglu. Local histogram based segmentation using the Wasserstein distance. *International Journal of Computer Vision*, 84(1):97–111, 2009.
- [37] M. Nikolova. Minimizers of cost-function involving nonsmooth data-fidelity terms. *SIAM Journal on Numerical Analysis*, 40(3):965–994, 2004.
- [38] M. Nikolova. Weakly constrained minimization: application to the estimation of images and signals involving constant regions. *Journal of Mathematical Imaging and Vision*, 21(2):155–175, 2004.
- [39] A. Oliva and A. Torralba. Modeling the shape of the scene: a holistic representation of the spatial envelope. *International Journal of Computer Vision*, 42(3):145–175, 2001.
- [40] S. Osher, A. Solé, and L. Vese. Image decomposition and restoration using total variation minimization and the  $h^1$ . *Multiscale Modelling and Simulation*, 1(3):349–370, 2003.
- [41] K. Papafitsoros and C. Schonlieb. A combined first and second order variational approach for image reconstruction. *Journal of Mathematical Imaging and Vision*, 2013.
- [42] P. Perona and J. Malik. Scale-space and edge detection using anisotropic diffusion. *IEEE Transactions on Pattern Analysis and Machine Intelligence*, 12(7):629–639, 1990.
- [43] L. Pizarro, P. Mrazek, S. Didas, S. Grewenig, and J. Weickert. Generalised nonlocal image smoothing. *International Journal of Computer Vision*, 90(1):62–87, 2010.
- [44] V. B. S. Prasath. Color image segmentation based on vectorial multiscale diffusion with inter-scale linking. In *Third International Conference on Pattern Recognition and Machine Intelligence (PReMI-09)*, pages 339–344, Delhi, India, December 2009. Springer LNCS 5909 Eds.: S. Chaudhury, S. Mitra, C. A. Murthy, P. S. Sastry, Sankar K. Pal.
- [45] V. B. S. Prasath and A. Singh. A hybrid convex variational model for image restoration. *Applied Mathematics and Computation*, 215(10):3655–3664, 2010.
- [46] V. B. S. Prasath and A. Singh. Well-posed inhomogeneous nonlinear diffusion scheme for digital image denoising. *Journal of Applied Mathematics*, 2010:14pp, 2010. Article ID 763847.
- [47] V. B. S. Prasath and A. Singh. An adaptive anisotropic diffusion scheme for image restoration and selective smoothing. *International Journal of Image and Graphics*, 12(1):18pp, 2012.
- [48] V. B. S. Prasath and D. Vorotnikov. On a system of adaptive coupled PDEs for image restoration. *Journal of Mathematical Imaging and Vision*, 48(1):35–52, 2014.
- [49] L. Rudin, S. Osher, and E. Fatemi. Nonlinear total variation based noise removal algorithms. *Physica D*, 60(1–4):259–268, 1992.

- [50] B. Russell, A. Torralba, K. Murphy, and W. T. Freeman. LabelMe: a database and web-based tool for image annotation. *International Journal of Computer Vision*, 77(1–3):157–173, 2007.
- [51] D. Strong. *Adaptive total variation minimizing image restoration*. PhD thesis, UCLA Mathematics Department, USA, August 1997.
- [52] D. M. Strong and T. F. Chan. Spatially and scale adaptive total variation based regularization and anisotropic diffusion in image processing. Technical Report 96–46, UCLA CAM, 1996.
- [53] E. Tadmor, S. Nezzar, and L. Vese. A multiscale image representation using hierarchical  $(BV, L^2)$  decomposition. *Multiscale Modeling and Simulation*, 2(4):554–579, 2004.
- [54] L. Tang and C. He. Multiscale texture extraction with hierarchical  $(BV, G_p, L^2)$ . *Journal of Mathematical Imaging and Vision*, 45(2):148–163, 2013.
- [55] L. Vese and T. F. Chan. Image denoising and decomposition with total variation minimization and oscillatory functions. *Journal of Mathematical Imaging and Vision*, 20(1–2):7–18, 2004.
- [56] L. Vese and S. Osher. Modeling textures with total variation minimization and oscillating patterns in image processing. *Journal of Scientific Computing*, 19(1–3):553–572, 2003.
- [57] Z. Wang, A. C. Bovik, H. R. Sheikh, and E. P. Simoncelli. Image quality assessment: from error visibility to structural similarity. *IEEE Transactions on Image Processing*, 13(4):600–612, 2004.
- [58] W. Yin, D. Goldfarb, and S. Osher. Image cartoon-texture decomposition and feature selection using the total variation regularized  $L^1$  functional. In *Variational, Geometric, and Level Set Methods in Computer Vision*, pages 73–84, Beijing, China, 2005. Lecture Notes in Computer Science Vol. 3752 (Eds. N. Paragios, O. Faugeras, T. Chan and C. Schnörr).
- [59] W. Yin, D. Goldfarb, and S. Osher. The total variation regularized  $L^1$  model for multi scale decomposition. *Multiscale Modeling and Simulation*, 6(1):190–211, 2006.
- [60] V. G. Zvyagin and D. A. Vorotnikov. *Topological approximation methods for evolutionary problems of nonlinear hydrodynamics*, volume 12 of *de Gruyter Series in Nonlinear Analysis and Applications*. Walter de Gruyter & Co., Berlin, Germany, 2008.